Numerical Simulation of High Energy Density Plasmas in KALIF Beam-Target Interaction Experiments

J.J. MacFarlane and P. Wang

December 1995

UWFDM-1002

FUSION TECHNOLOGY INSTITUTE

UNIVERSITY OF WISCONSIN

MADISON WISCONSIN

Numerical Simulation of High Energy Density Plasmas in KALIF Beam-Target Interaction Experiments

J. J. MacFarlane and P. Wang

Fusion Technology Institute
University of Wisconsin-Madison
1500 Engineering Drive
Madison, WI 53706

December 1995

UWFDM-1002

Contents

1. Introduction

The purpose of this report is to provide a detailed description of theoretical and computational work performed during the 1995 calendar year in support of KALIF beam-plasma interaction experiments. This work has been concentrated primarily in two areas. First, we have performed collisional-radiative equilibrium (CRE), atomic physics, and radiation-hydrodynamics simulations to assist in the interpretation of measured x-ray spectra obtained in laser and proton beam-heated target experiments at FZK. These spectra were obtained in a preliminary set of experiments to test diagnostics and obtain initial K_α satellite spectra from targets heated by the KALIF proton beam. Second, we have calculated stopping powers and equation of state data using our unified self-consistent field code, which is based on a muffin tin model. A procedure has been developed to tabulate the results in a way which allows for efficient use by radiation-hydrodynamics codes.

Table 1.1 shows the list of tasks for our 1995 work with FZK. The first task was to perform simulations to interpret K_α spectra obtained in beam-plasma interaction experiments. This involved performing CRE and atomic physics calculations for intermediate–Z targets ($Z \approx 9 - 13$) to examine their K_α spectra, and in particular the magnitude of the emission line fluxes for the various targets. Calculations were also performed for laser-heated targets to examine their spectra and the absolute intensities from various K-shell lines. One of the goals for this work was to try to understand why x-ray line emission could be observed for laser-heated Na, but not for proton-heated Na targets using the B_θ diode.

Simulations were also performed to predict the time-integrated K_α spectra for Al using proton beam parameters for the B_θ diode. To do this, radiation-hydrodynamics simulations were performed to predict the time- and space-dependent temperature and density within the target. K_α spectra were then calculated at a number of simulation times, using the plasma conditions predicted from the radiation-hydrodynamics simulations as well at the time-dependent proton beam voltage and current density. The predicted time-integrated K_α satellite spectrum was found to be in qualitative agreement with initial spectral measurements for Al. It was also found that K_α emission line intensities at relatively late times in the proton beam pulse drop significantly due to the decrease in the beam voltage. This suggests that absorption spectroscopy may provide significantly better constraints for determining the *late-time* target plasma conditions in KALIF proton beam experiments.

The second task concerns the development and application of atomic physics models for studying ion beam-heated plasmas. Improvements were made to our new stopping power

algorithm, which is a self-consistent field model based on a muffin tin potential. In addition, we have developed a procedure to fit the results from the stopping power calculations to a simple analytic formula which can be efficiently used in radiation-hydrodynamics codes. This procedure has been implemented and tested in our 1-D radiation-hydrodynamics code BUCKY-1. Equation of state data are computed using a hybrid muffin tin/DCA (detailed configuration accounting) model. This data is used by radiation-hydrodynamics codes using a table lookup procedure. BUCKY-1 simulations utilizing these equations of state typically conserve energy to within 1-2%.

Table 1.1. Tasks for 1995

1. Perform analysis of K_α spectral data obtained in KALIF beam-plasma interaction experiments.
   (a) Perform collisional-radiative equilibrium (CRE) to predict x-ray line spectra for KALIF experiments.
   (b) Perform ATBASE calculations to set up atomic cross section tables for spectral analysis.
   (c) Post-process radiation-hydrodynamics simulations to predict time-integrated K_α emission spectra.
   (d) Predict plasma temperatures and densities from the intensity ratios of K_α emission lines.
2. Compute ion stopping powers and equations of state data using self-consistent field muffin tin model. Put in format which can be utilized by KATACO radiation-hydrodynamics code.
3. Document results in Final Report to FZK. Supply FZK with updated CRE and ATBASE codes.

2. Calculations of X-ray Spectra for Laser and Proton Beam-Heated Target Experiments

X-ray spectra were obtained in a preliminary set of target heating experiments during the past year at FZK. Targets containing Al, Mg, Na, and F were irradiated in proton beam experiments using the B_θ diode. Proton-induced K_α emission lines were observed for Al and Mg, but were not observed for Na or F. However, when NaF targets were heated by a laser beam, K-shell emission lines were observed. In some cases, dielectronic recombination satellites to the K-shell resonance lines were also observed.

Below, we describe a series of calculations which were performed to assist in the interpretation of these preliminary experimental results. A first question to address is whether it should be expected that the K_α line intensities are lower for lower-Z species. That is, is the lack of a detectable K_α spectrum for Na and F due to them having lower emission intensities, or is it due to an instrumental effect? To examine this question, we performed a series of collisional-radiative equilibrium (CRE) calculations to examine the K_α satellite spectra of Na and Al as a function of proton beam voltage and target plasma temperature. These results are presented in Section 2.1.

Second, since Na emission lines were observed in the laser experiments, but not in the B_θ diode experiments, one can ask how much higher should we expect the emission intensities to be in the laser experiments? To address this question, we performed radiation-hydrodynamic simulations of laser-heated Na targets to estimate the temperatures and densities in the high-temperature emission region. CRE calculations were then performed to estimate the K-shell line intensities. These results are then compared with the K_α satellite line fluxes computed for (B_θ diode) proton-irradiated targets. These results are described in Section 2.2.

Finally, we performed simulations to predict the time-integrated spectrum for an Al target heated with the B_θ diode proton beam. This is done by first performing 1-D radiation-hydrodynamic simulations of the Al target heating and expansion. Then, a series of CRE calculations were performed using the time- and space-dependent values of the plasma temperature, plasma density, proton beam kinetic energy, and proton current density predicted from the radiation-hydrodynamics calculation at selected simulation times. In particular, we have examined the magnitude of the K_α line intensities as a function of time. Results from these simulations are presented in Section 2.3.

2.1. Comparison of K_α Line Intensities for Al and Na Targets

In this section, we describe results from CRE and atomic physics calculations concerning the difference in magnitude of the K_α line intensities for Na and Al. In initial KALIF B_θ diode experiments, the K_α intensities for Mg inferred from spectroscopic measurements were approximately a factor of 5 lower than for Al. For Na, the flux levels were too low to be observed. The purpose of the calculations is to determine whether this is due to lower K_α fluxes for the lower-Z targets, or whether it might be caused by some instrumental effect.

Figure 2.1 shows the total flux — integrated over the K_α spectral region for each material — for Al and Na targets plotted as a function of the proton beam voltage. In each case, the ion density was 6×10^{19} cm^{-3}, the temperature was $T = 10$ eV, and the plasma thickness corresponded to a foil pre-expansion thickness of 6 μm. At each voltage it is seen that the K_α fluxes of the 2 materials are similar, with differences being less than a factor of 2 in all cases (that is, much smaller than the Mg and Al flux differences inferred from the experiments).

The reason the K_α intensities increase with increasing beam voltage can be seen in Fig. 2.2, which shows the proton-impact ionization cross sections for K-shell electrons of Na and Al. For both materials the cross section shows a strong monotonically increasing dependence on voltage for $E_B \lesssim 2$ MeV. Although the Na cross section is roughly a factor of 2 higher, K_α line intensities are proportional to the product of the proton-impact ionization cross section and the fluorescence yield. Since the fluorescence yields for Al are substantially higher than those for Na ($\sim 5\%$ vs. 3%), their K_α fluxes are of similar magnitude.

Figure 2.3 shows the dependence of the total K_α fluxes for Al and Na as a function of temperature. The simulations were identical to those in Fig. 2.1; however, in this case the temperature was varied while the beam voltage was held constant at 1.0 MeV. Again, it is seen that the fluxes are of similar magnitude. For both materials the fluxes drop somewhat with increasing temperatures. Recent simulations indicate that at low temperatures, both opacity effects and multiple ionization effects due to the beam are unimportant. At higher temperatures ($T \gtrsim 5$ eV for Na) resonant self-absorption effects become important because states with $2p$ vacancies are heavily populated. However, the flux tends to remain relatively high in the simulations due to multiple ionization effects. The role of multiple ionization for these relatively thick targets will be investigated in more detail in future calculations.

To conclude, these results suggest it is unlikely that order of magnitude differences exist in the K_α fluxes from Na and Al targets of similar dimensions.

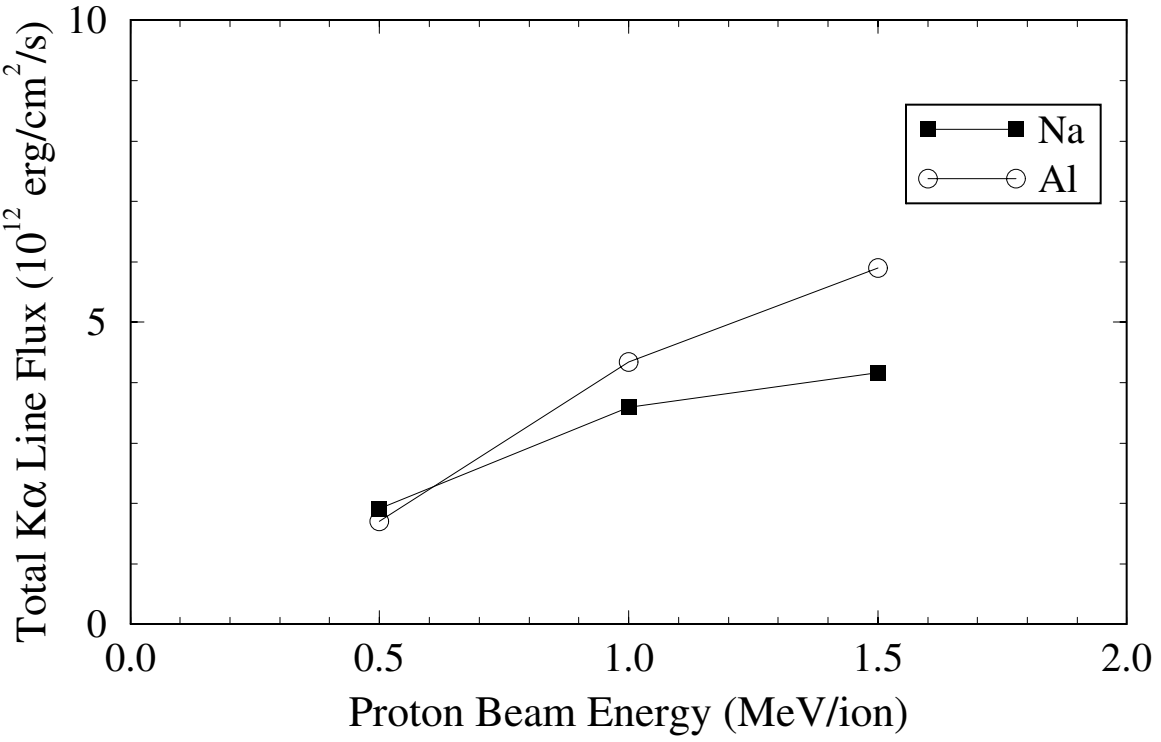

Figure 2.1. Beam voltage dependence of emergent flux from Na and Al targets frequency-integrated over the K_α spectral region of each material. In each case, $T = 10$ eV, $n = 6 \times 10^{19}$ ions/cm^3 and $\Delta L_{\rm orig} = 6\,\mu$m.

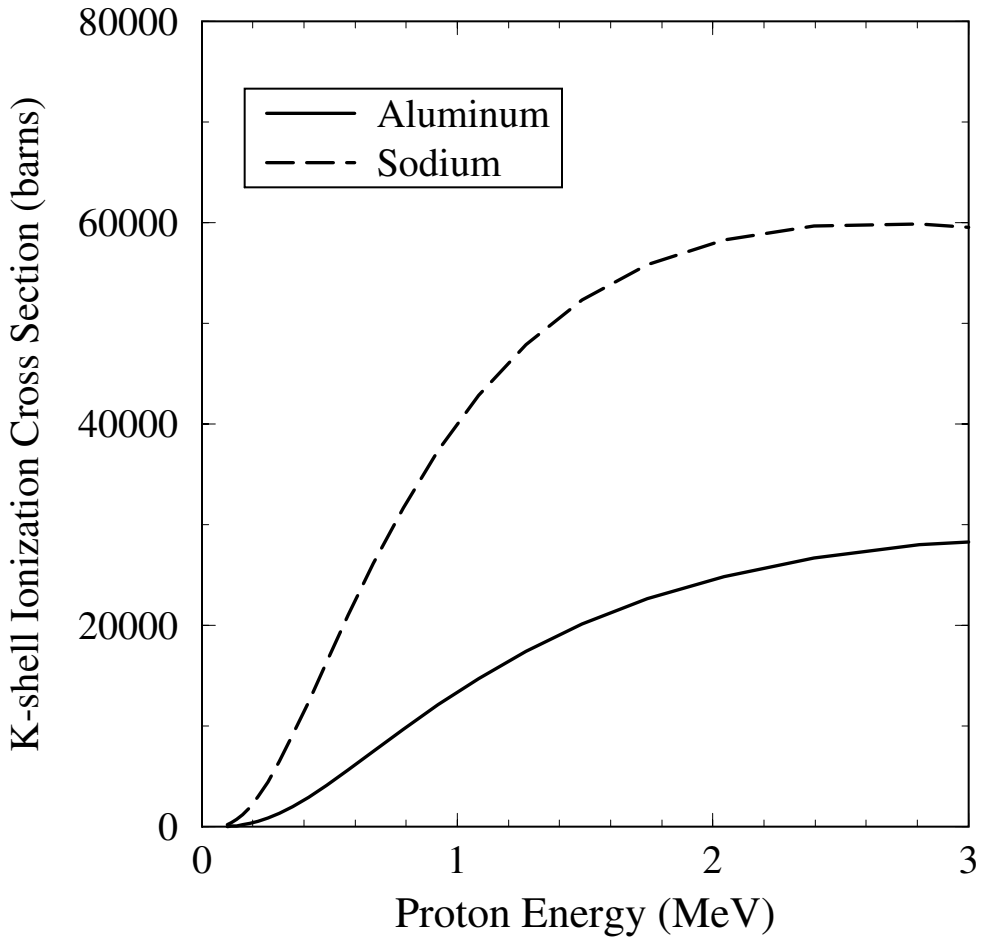

Figure 2.2. Proton-impact ionization cross sections vs. beam voltage for K-shell electrons of Na and Al.

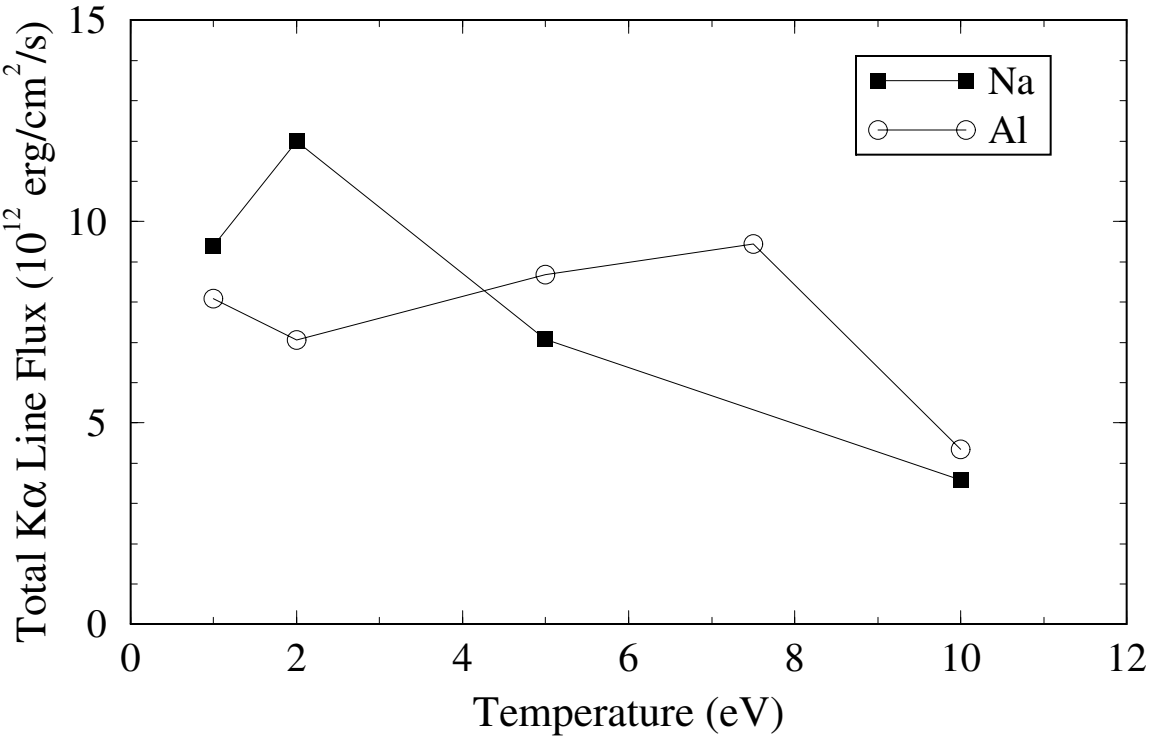

Figure 2.3. Temperature dependence of emergent flux from Na and Al targets frequency-integrated over the K_α spectral region of each material. In each case, $n = 6 \times 10^{19}$ ions/cm^3, $\Delta L_{\rm orig} = 6\,\mu$m, and $E_{\rm beam} = 1.0$ MeV.

2.2. K-Shell Spectra Predicted for Laser-Heated Targets

To make a comparison of the x-ray line intensities for laser and ion beam-heated targets, we have performed a series of radiation-hydrodynamics and CRE calculations for parameters relevant to the FZK experiments. The purpose of these simulations is to help explain why Na K-shell spectra were observed in diagnostic test experiments using a laser-heated target, but were not observed in initial KALIF experiments using the B_θ diode.

BUCKY-1 radiation-hydrodynamics [1] simulations were performed for laser power densities ranging from 1 TW/cm^2 to 40 TW/cm^2. For a laser energy of 6 J in a 7 ns pulse, this corresponds to a spot size (diameter) of $D \approx 50 - 300\,\mu$m. The laser pulse was assumed to be flat-topped, and incident on a planar Na target. The target thickness was assumed to be large ($\sim 150\,\mu$m). The actual thickness is unimportant, however, because the x-ray spectra were observed from the side of the target irradiated by the laser. In these simulations, radiation was transported using a multigroup, multiangle short characteristics model. Equation of state and opacity data tables for Na were computed using EOSOPA [2].

Figure 2.4 shows the temperature and density distributions predicted at simulation times of 2, 4, and 6 ns in the $P_L = 1$ TW/cm^2 calculation. In the top figure the electron and ion temperatures are indicated by the solid and dashed curves, respectively. Throughout the majority of the laser pulse, the electron temperatures are in the range of 200 to 300 eV. At the bottom, the densities in the high-temperature region — that is, the region emitting the x-rays — is seen to be $\sim 10^{-3}$ g/cm^3.

Figure 2.5 shows similar plots for the $P_L = 10$ TW/cm^2 case. Here, it is seen that the electron temperatures are approximately 0.7 to 1.0 keV throughout much of the laser pulse. The densities in the high-temperature blowoff region are again low ($\sim 10^{-3}$ g/cm^3). However, in this case, we have plotted the density distributions on a linear scale to show the strong shock that is generated and propagates into the cold region of the target. (Note the mass scales in the top and bottom plots are different.)

From the radiation-hydrodynamics results we conclude that the plasma conditions in laser-heated Na were roughly in the temperature range of 0.2–1.0 keV and density range of $10^{-4} - 10^{-2}$ g/cm^3.

K-shell spectra observed from laser-heated plasmas exhibit satellites on the long wavelength side of resonance lines which arise due to dielectronic recombination [3,4]. An example of this is the Li-like satellites next to the He$_\alpha$ line, which arise due to transitions of the type (see Figure 2.6):

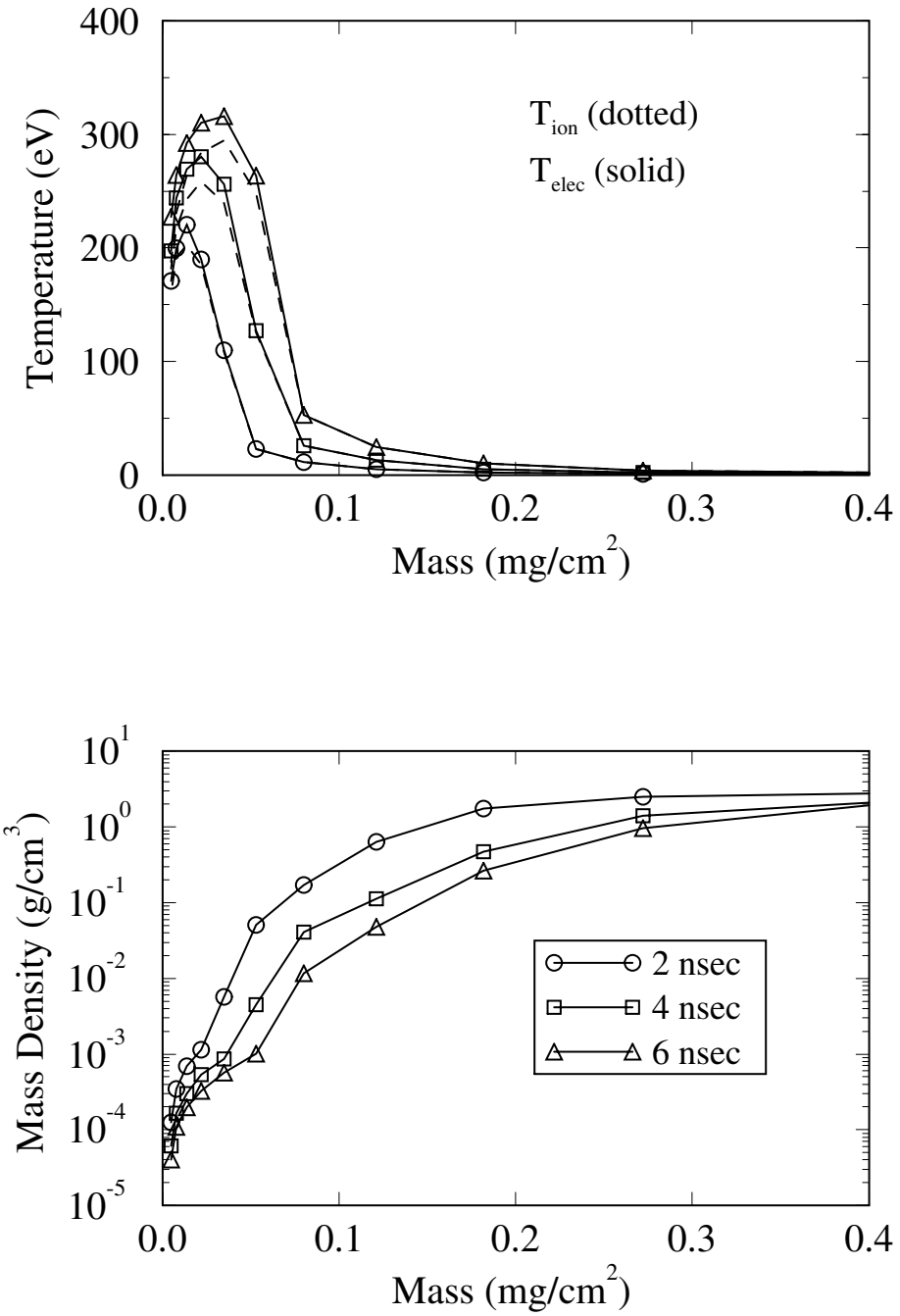

Figure 2.4. Temperature and density distributions computed from radiation-hydrodynamics simulations of a Na target heated by a $P_L = 1$ TW/cm^2, 7 ns laser pulse.

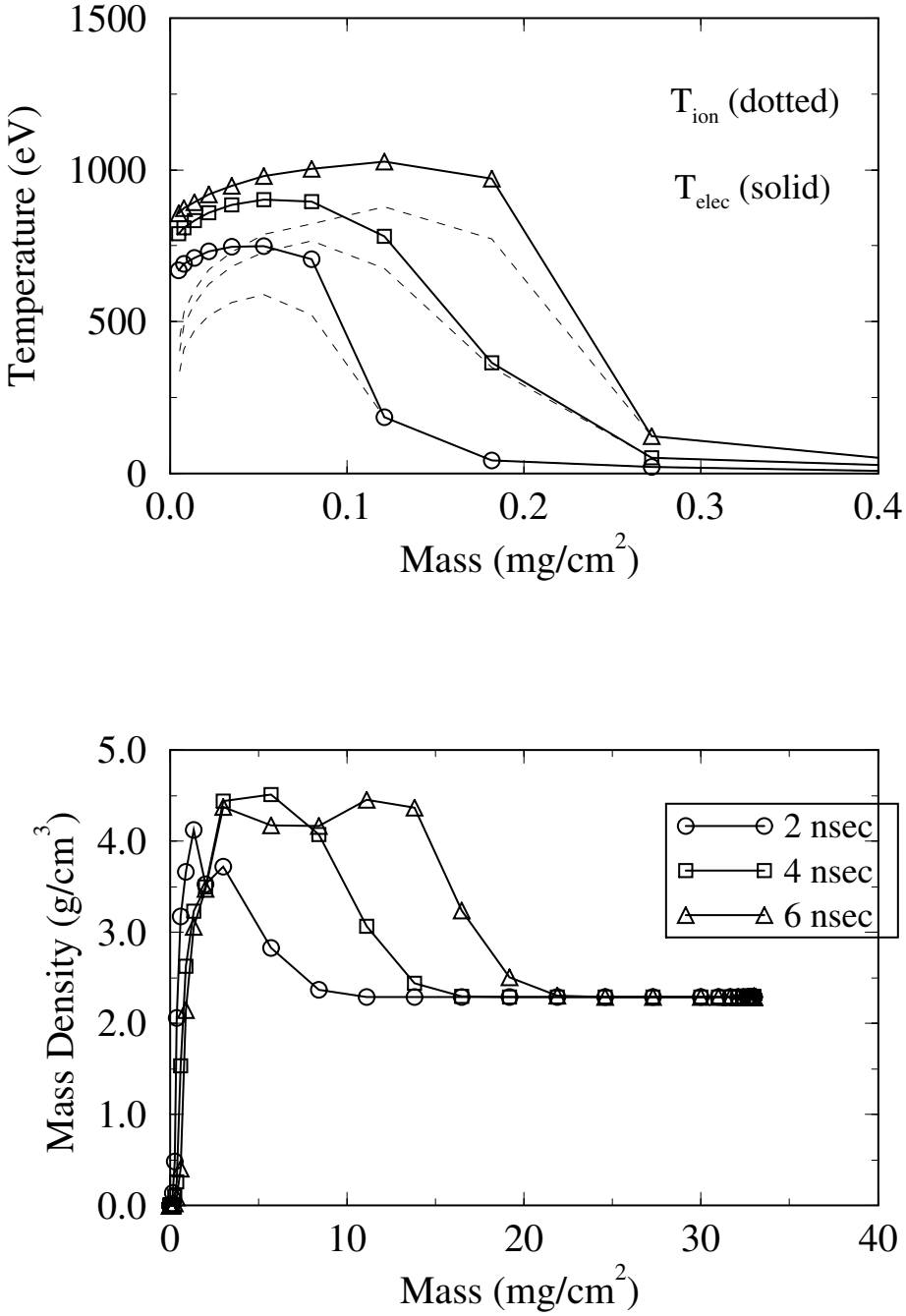

Figure 2.5. Same as Figure 2.4, but for a laser power of 10 TW/cm^2.

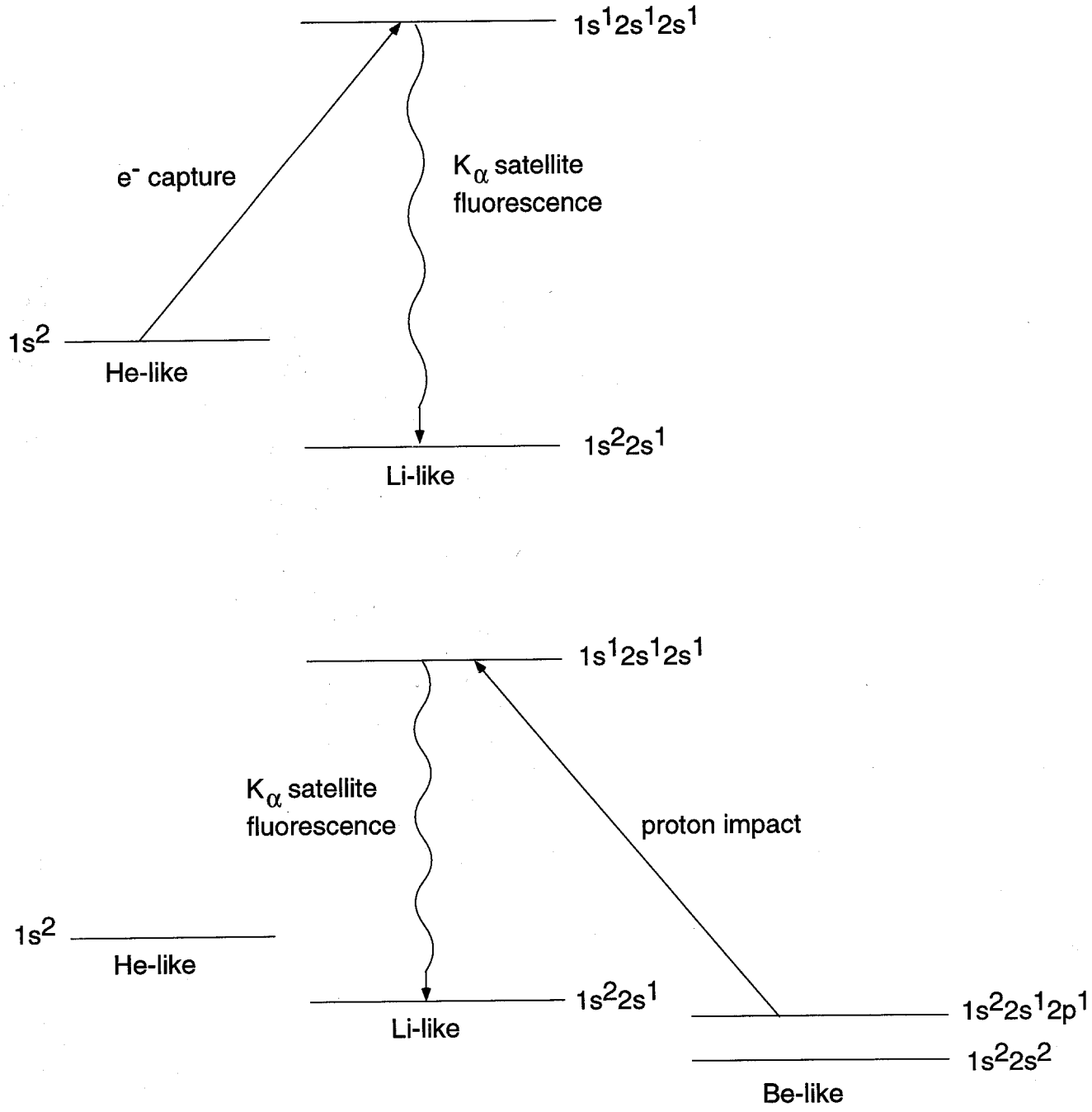

Figure 2.6. Energy level diagrams illustrating how satellites are produced in laser-produced plasmas by dielectronic recombination (top), and in proton beam-heated plasmas by ion-impact ionization (bottom).

$$1s^2 \xrightarrow{\text{e-capture}} > 1s^1 2s^1 2p^1 \xrightarrow[\text{decay}]{\text{radiative}} > 1s^2 2s^1 \,.$$

These features have been observed in several of the spectra obtained in the FZK laser experiments.

During the past year we have upgraded our CRE code (NLTERT [5]) to include electron capture transitions in order to compute dielectronic recombination satellite spectra. The electron capture transition rate is given by [6]:

$$n_e n_i \beta_{iu} = n_e n_i \, \frac{1}{2} \left(\frac{h^2}{2\pi m_e k T_e} \right)^{3/2} \, \frac{g_u}{g_i} \, e^{\Delta E / T_e} \, A^a_{ui} \,, \tag{2.1}$$

where n_e is the electron density, n_i is the density of the initial state ($1s^2$ in the above example), h and k are the Planck and Boltzmann constants, m_e and T_e are the electron mass and temperature, g_u and g_i are the statistical weights of the upper (autoionization) and initial states, ΔE is the transition energy, and A^a_{ui} is the autoionization rate. Note that Eq. (2.1) represents a detailed balance relation between electron capture and autoionization.

Using predictions from the radiation-hydrodynamics simulations as a guide, spectra were computed using NLTERT for Na plasmas of uniform temperature and density. Figure 2.7 shows the K-shell spectra computed for temperatures of 200, 400, and 600 eV. In each case the ion density was 10^{20} cm^{-3} ($\rho = 4 \times 10^{-3}$ g/cm^3) and the plasma thickness was 100 μm. The spectrum at $T = 600$ eV shows strong emission from both the L_α and He_α lines at 10.0 and 11.0 Å, respectively. Note that the satellites to the L_α line, which are due to $2p^1 2\ell^1 \rightarrow 1s^1 2\ell^1$ transitions ($\ell = s, p$), are also present. The satellites to the He_α line are fairly weak at 600 eV. As the temperature drops, the L_α intensity decreases. At $T = 200$ eV, the H-like lines are very weak compared to the He-like lines.

The satellite structure for the He_α spectral region is shown in more detail in Figure 2.8. The plasma conditions are the same as those in the previous figure. Note that the intensities of the satellites increase relative to the He_α line as the temperature drops. (Also note the change in scale.) At the higher temperatures, the satellites become weaker because of the shift to higher ionization. That is, the population of the $1s^2$ level, from which the dielectronic recombination satellites originate, decreases. This can also be seen in the shape of the He_α line at 11.0 Å, which shows very pronounced opacity broadening effects at the lower temperatures. The calculated mean charge states for these conditions are $\bar{Z} = 9.3$, 10.1, and 10.5 for $T = 200$, 400, and 600 eV, respectively.

Figure 2.9 shows a time-integrated spectrum obtained in one of the FZK laser-produced Na plasma experiments. Note the satellite structure is similar to those calculated

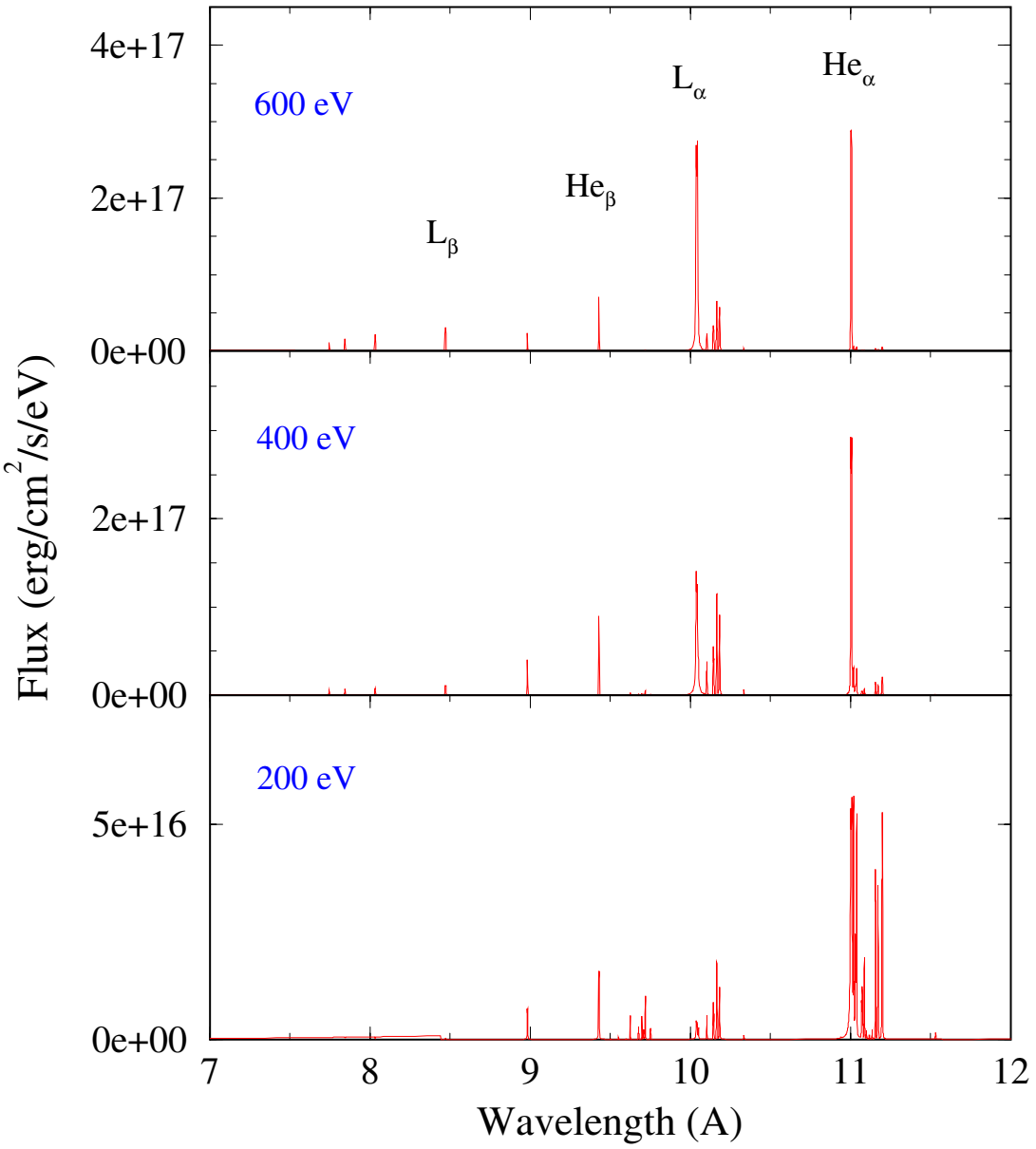

Figure 2.7. Calculated K-shell spectra for Na at $T = 200$, 400, and 600 eV. In each case, the density was $n = 1\times10^{20}$ ions/cm^3 and plasma thickness was $\Delta L = 100\mu$m.

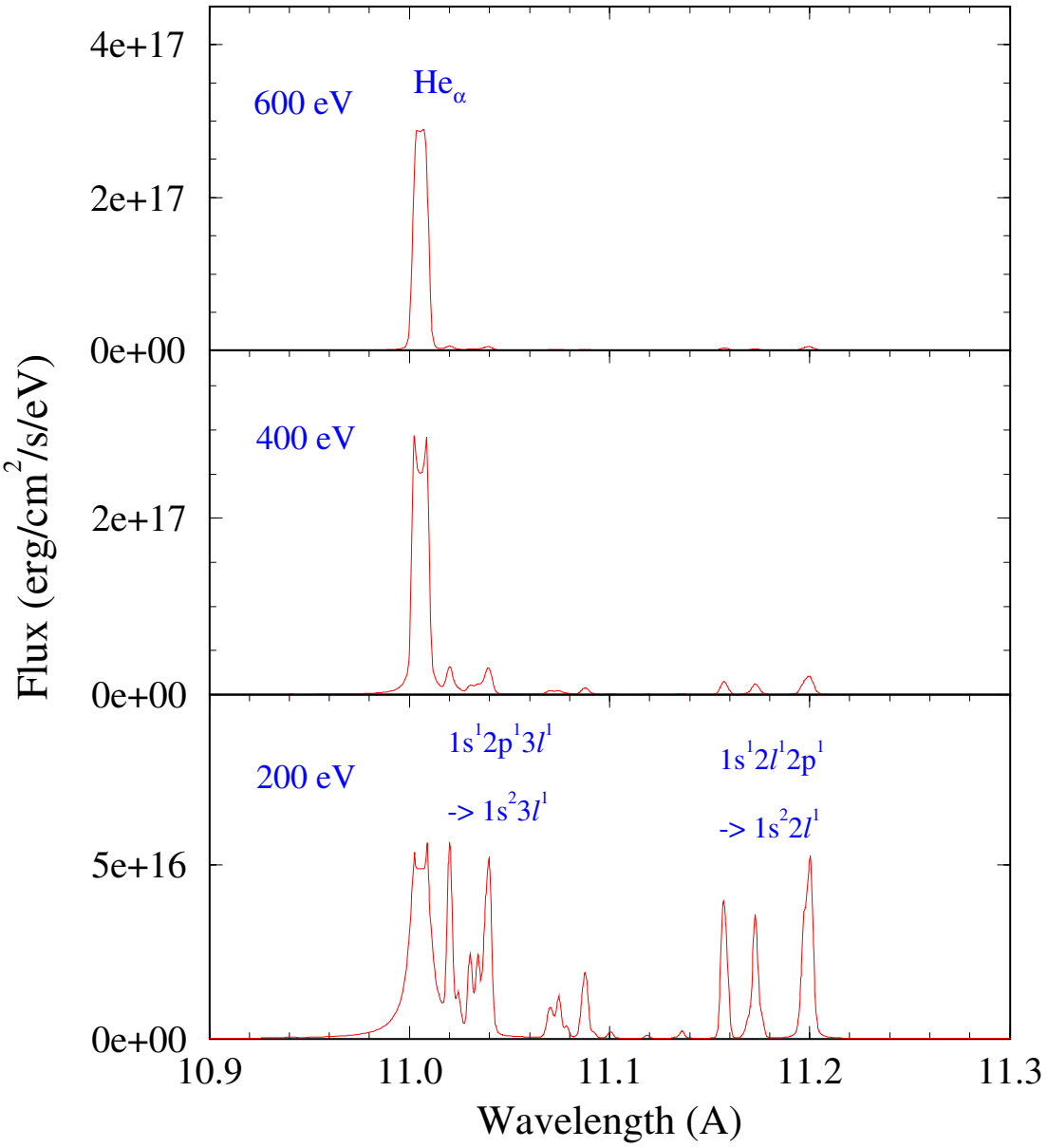

Figure 2.8. Same as Figure 2.8, but showing the dielectronic recombination satellite spectrum near the Na He$_\alpha$ line in more detail.

in the $T = 200 - 400$ eV range. In fact, for $T = 400$ eV, the He_α intensity is ~ 10 times higher than the satellite line intensities, which is in rough agreement with the experimental spectrum. Because of time- and space-integration effects in the measured spectrum, it is difficult to determine precisely the temperature. However, since our primary goal here is to estimate the magnitude of the line intensities, and compare them with those predicted for the ion beam experiments, we note that the calculated intensities of the satellites at $T = 400$ eV are $\sim 2 \times 10^{16}$ erg/cm^2/s/eV. The intensity of the He_α line is $\sim 2 \times 10^{17}$ erg/cm^2/s/eV.

To estimate the space- and time-integrated flux, we assume a characteristic time of 7 ns (i.e., the laser pulse duration). In the hydrodynamics calculations, we note that a peak temperature of 300 eV was achieved using a laser power of $P_L = 1$ TW/cm^2. This corresponds to a spot diameter of $D = 330\,\mu$m. It is of course possible that the diameter of the emission region could be larger due to plasma expansion (multidimensional) effects. It, however, seems unlikely that the size of the emission region was much less than $D = 100$ μm, which corresponds to the $P_L = 10$ TW/cm^2 case. Using $D = 200$ μm, the flux in the He_α line is:

$$\begin{aligned} \int\int F_\nu dA\, dt &\cong (2 \times 10^{17}\ \mathrm{erg/cm^2/s/eV})(7\ \mathrm{ns})(\pi) \left(\frac{200\,\mu\mathrm{m}}{2}\right)^2 \\ &= 4.4 \times 10^5\ \mathrm{erg/eV}\,. \end{aligned}$$

The calculated satellite fluxes are roughly a factor of 10 lower.

These estimates of the laser-produced plasma K-shell time- and space-integrated fluxes are a factor of ~ 30–40 higher than the experimental values (see Fig. 2.9). The reason for this discrepancy is not clear at this time. However, we note that these results, along with those in Section 2.1, are consistent with a scenario in which the observed fluxes are degraded due to an intervening absorber (e.g., a filter) or a lower than expected instrument sensitivity. The optical depth required for a reduction of 30 – 40 in the flux is 3.4 – 3.7.

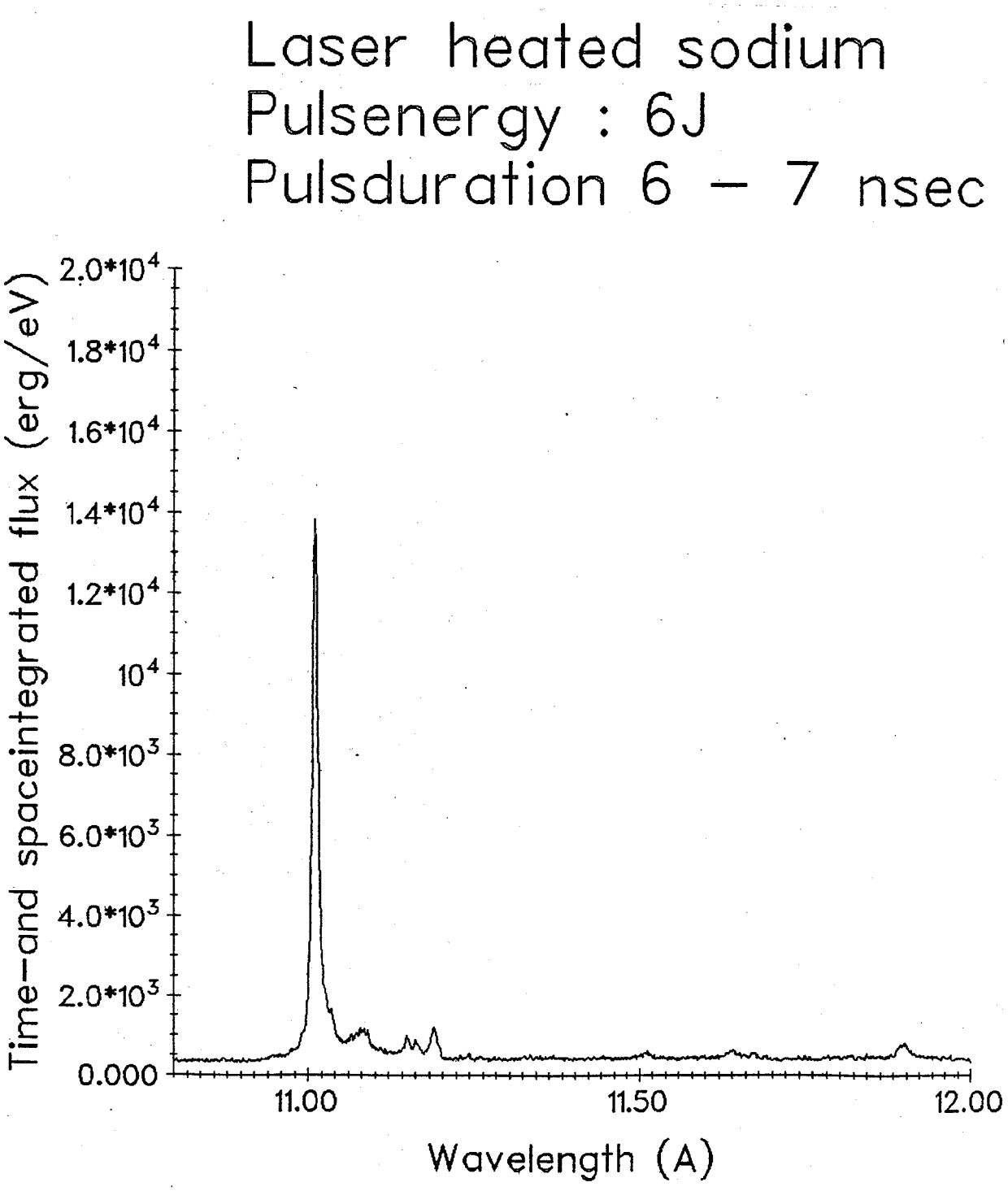

Figure 2.9. Experimental time-integrated spectrum for a laser-produced Na plasma obtained in FZK experiments.

2.3. Calculated K_α Spectra for B_θ Diode Experiments

Radiation-hydrodynamics and collisional-radiative equilibrium calculations were performed to predict the time-integrated K_α satellite spectrum from an Al target. The hydrodynamics simulations utilized time-dependent beam voltages and power densities for the B_θ diode (see Fig. 2.10). The calculations were performed for a 1 μm-thick Al foil using a stopping power model based on the work of Mehlhorn [7]. It is worth noting that calculations using the more recent stopping power model of Wang and Mehlhorn [8] gave very similar results for Al.

Figure 2.11 shows the temperature and density distributions in the Al plasma at simulation times of 40, 60, and 80 ns. Figure 2.12 shows the mass-weighted average temperature as a function of time. For the first 40 ns of the beam pulse, the temperature of the Al remains below 10 eV. Note that the peak power density of the proton beam occurs at $t = 40$ ns. At later times the temperature continues to increase to a maximum of $T = 28$ eV. The target continues to be heated at late times because: (1) the beam current used in the simulation remains relatively flat at late times, and (2) the beam voltage drops, which leads to a higher stopping power. This is shown in Fig. 2.13, which shows the beam voltage, current density, and average stopping power ($\langle dE/dx \rangle$) in the Al plasma as a function of time. Note that the stopping power increases rapidly at late times. Thus, even though the beam power density decreases significantly at late times there can still be substantial heating. This suggests that accurate measurement of the beam current and voltage at late times will be important in the analysis of target heating experiments.

Using space- and time-dependent predictions for temperature, density, beam current, and beam voltage, CRE calculations were performed to predict the K_α satellite spectra at every 10 ns of the beam pulse. Results for the K_α emission spectra are shown in Fig. 2.14. Note the change in scale of the ordinate at each time. The spectra also include instrumental broadening with $\lambda/\Delta\lambda = 1000$. For the first 40 ns of the beam pulse (i.e., when $T \lesssim 10$ eV), the "cold" (F-like) and O-like satellites exhibit the strongest emission. At $t \simeq 20 - 40$ ns the magnitude of the flux is $F_\nu \simeq 3 - 8 \times 10^{11}$ erg/cm^2/s/eV. At later times the target becomes hotter and the emission originates from higher and higher ionization stages. At $t \simeq 70{-}80$ ns, B-like and C-like lines exhibit the strongest emission. However, the intensities of the lines are substantially less than those at early times.

The decrease in intensity at late times in these simulations is primarily due to the dependence of the proton-impact ionization cross sections on the beam voltage. This can be seen by examining the K-shell ionization cross sections for protons on Al (see Fig. 2.2). Recall from Fig. 2.13 that the proton voltage *in the Al plasma* drops from about 1.4 MeV

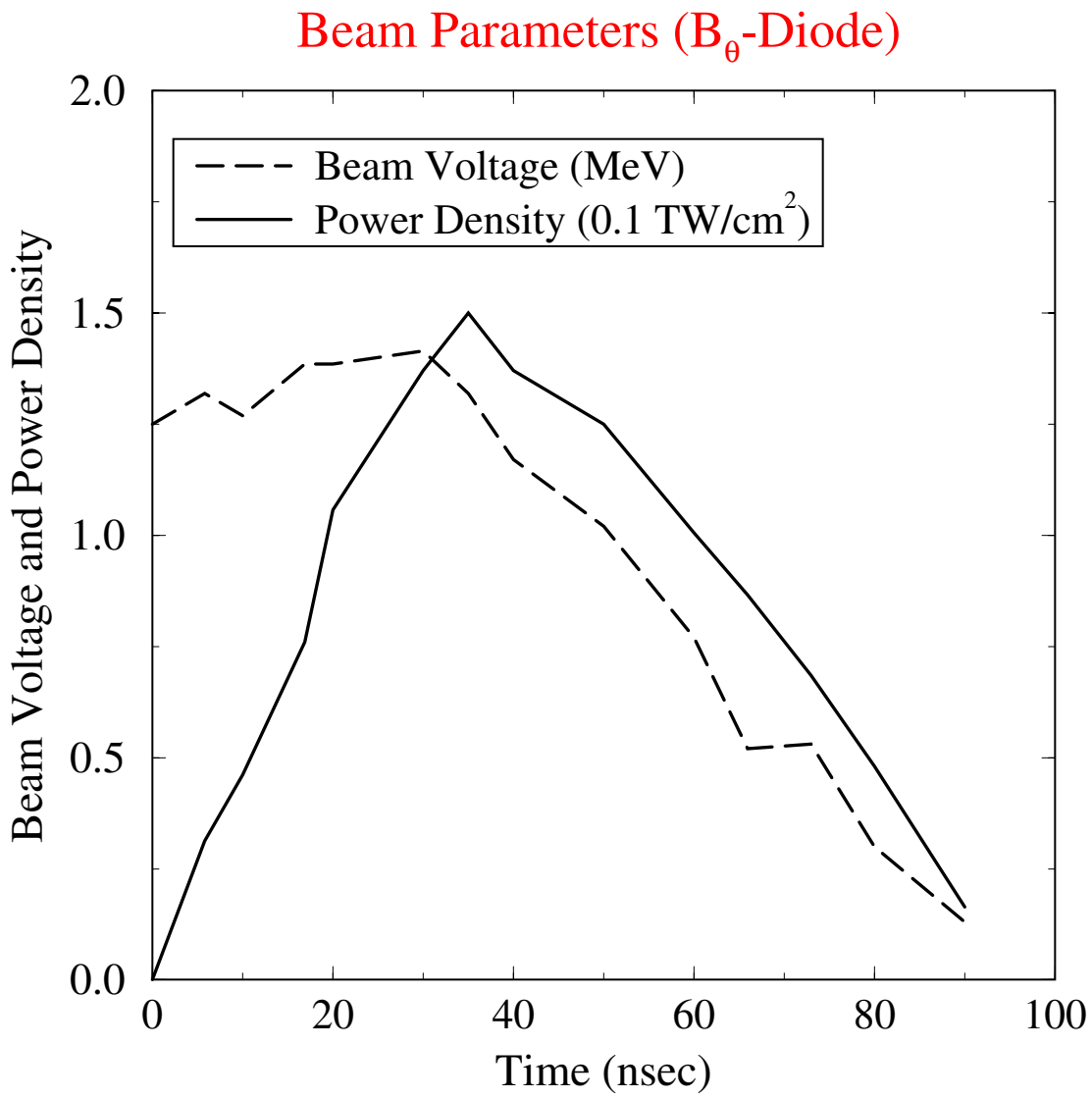

Figure 2.10. Time-dependent proton beam power density and voltage profiles used in radiation-hydrodynamics simulations of KALIF B_θ diode experiments.

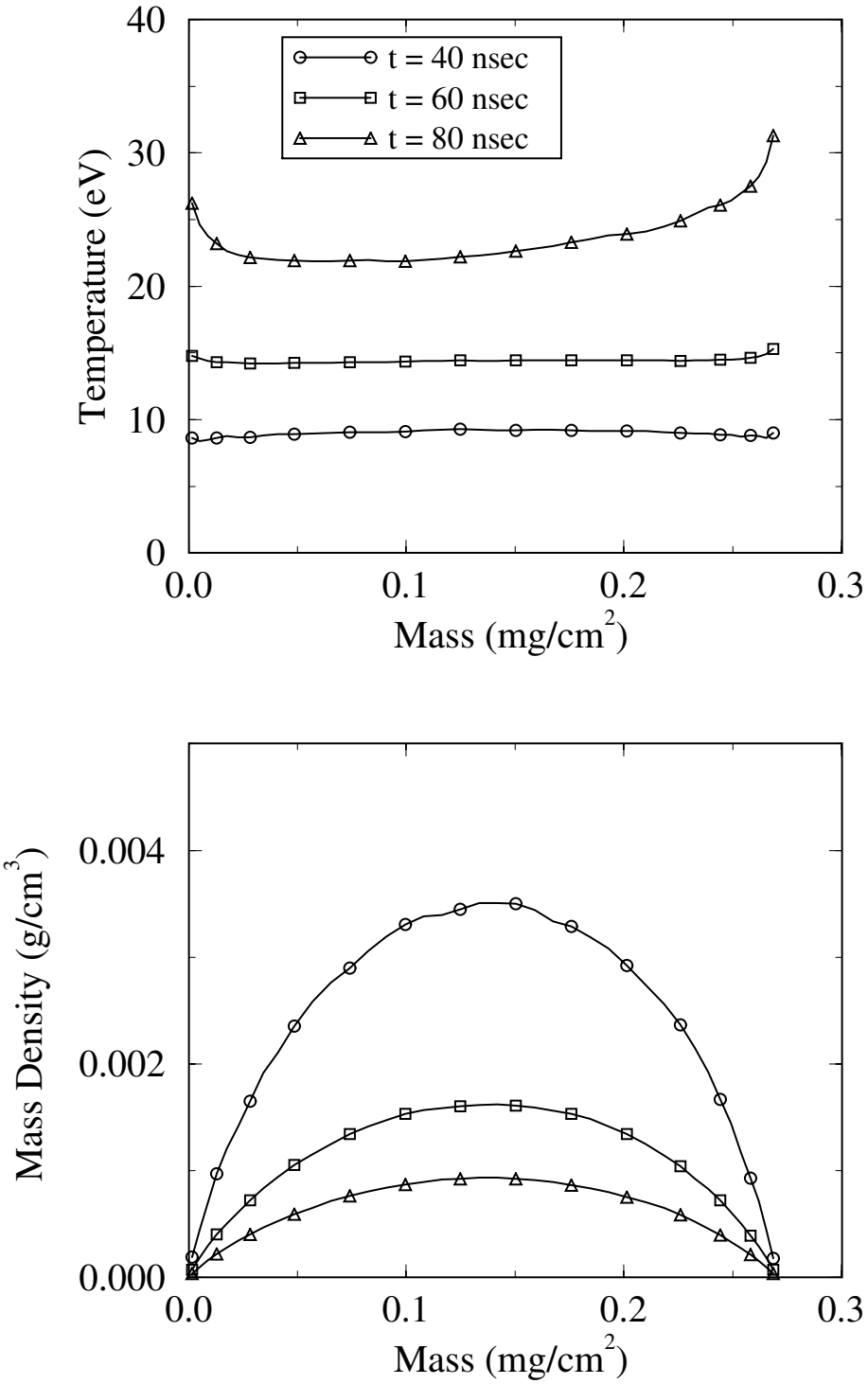

Figure 2.11. Temperature and density distributions in Al target plasma at $T = 40$, 60, and 80 ns for the B_θ diode radiation-hydrodynamics simulation.

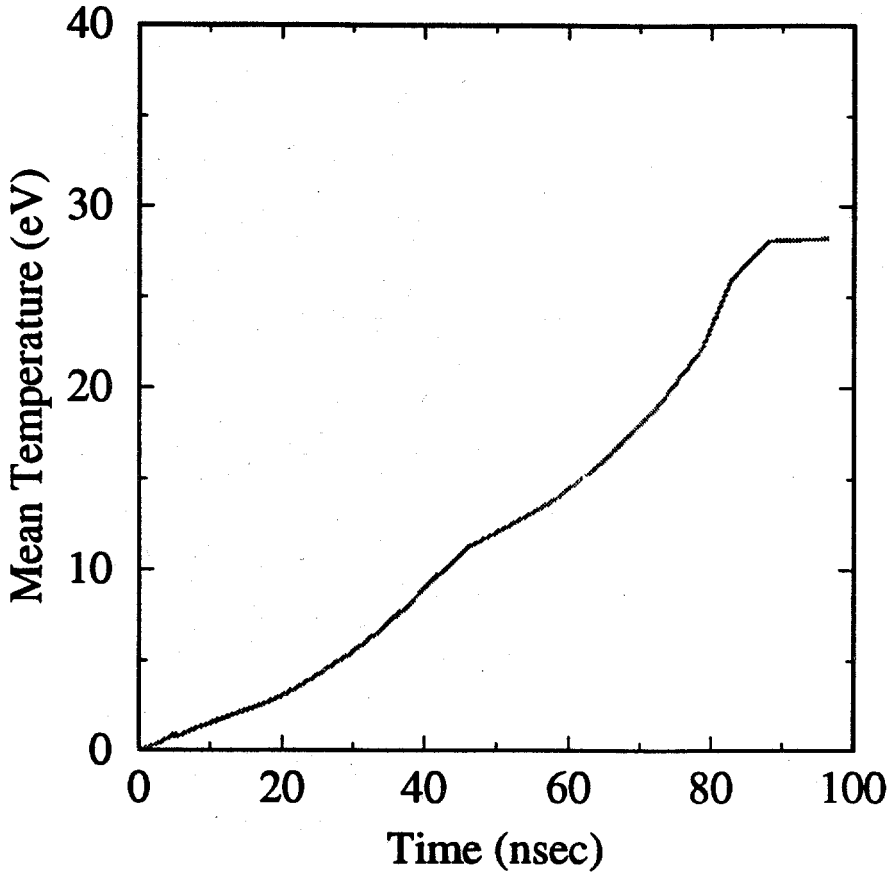

Figure 2.12. Average temperature of Al target plasma vs. time for B_θ diode simulation.

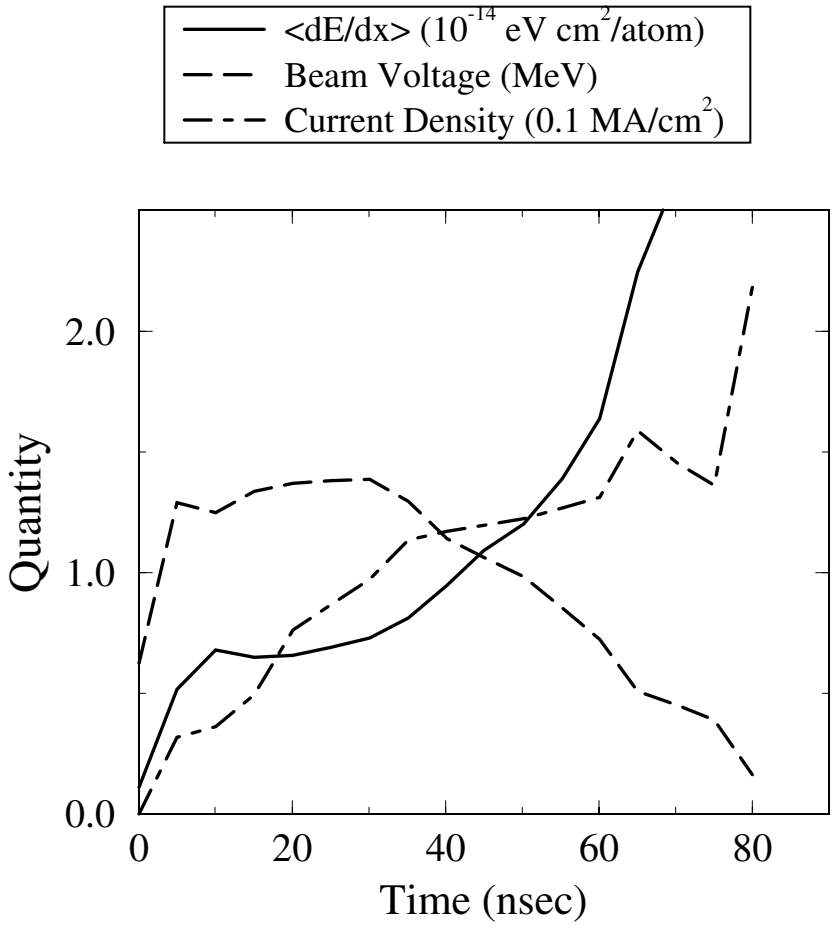

Figure 2.13. Time dependence of average stopping power, beam current density, and proton beam kinetic energy within the Al target computed for the B_θ diode simulation.

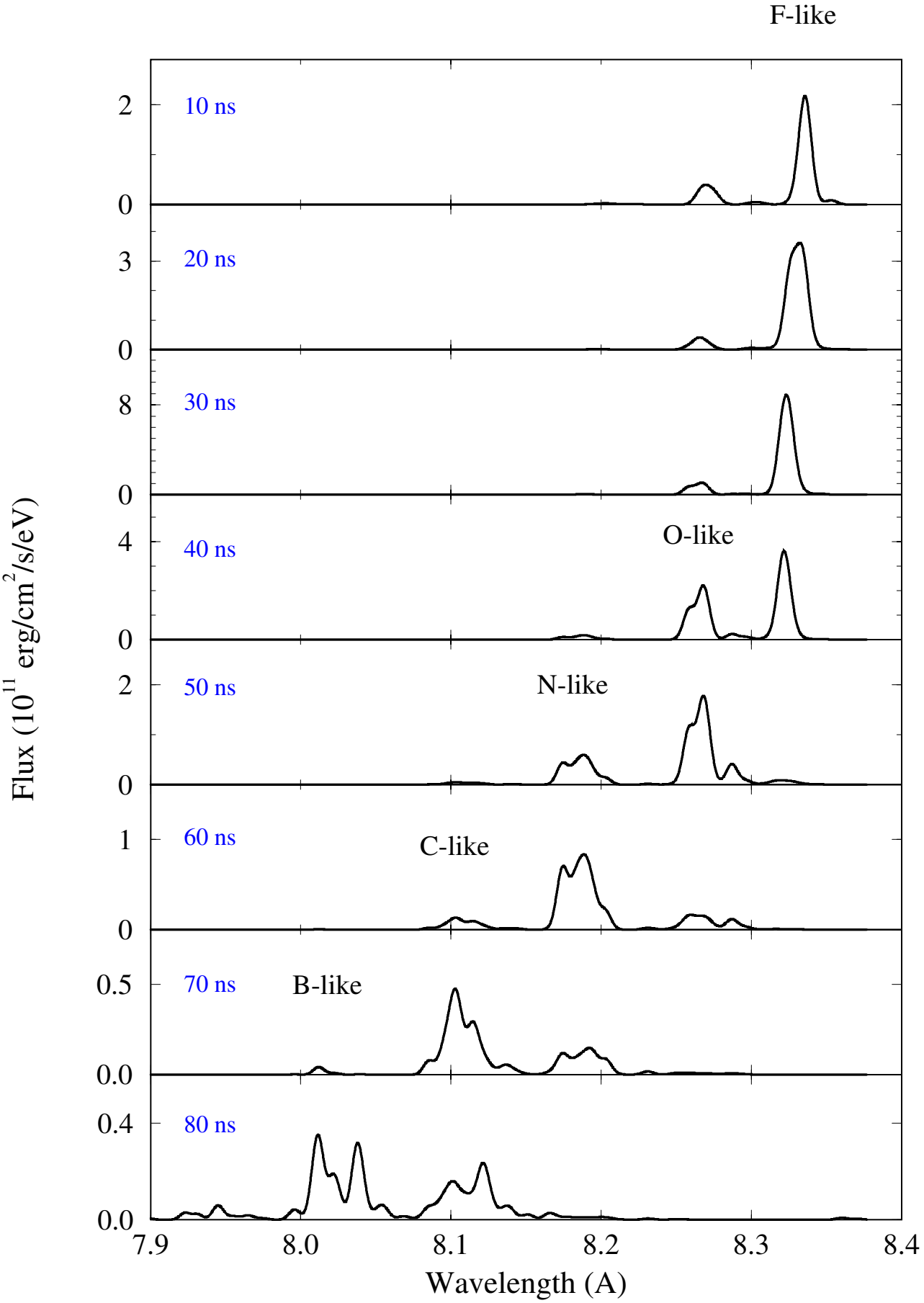

Figure 2.14. Calculated K_α satellite emission spectra at 10 ns time intervals for the B_θ biode simulation.

at 30 ns to about 0.5 MeV at 65 ns. This corresponds to a decrease in the proton-impact ionization cross section of roughly a factor of 5. This in turn leads to lower K_α satellite line intensities because their flux is proportional to the K-shell cross sections.

The time-integrated K_α emission spectrum is shown in Fig. 2.15. The top and bottom plots are the same spectra on different scales. Shown are curves integrated up to simulation times of 20, 40, 60, and 80 ns. The spectra show that the F-like ($\lambda = 8.34$ Å) and O-like ($\lambda = 8.27$ Å) features are the strongest, and that their emission occurs primarily within the first 40 ns of the beam pulse. Emission from the higher ionization stages occurs at later times and is substantially weaker. Because of the weaker emission at later times it can be difficult to accurately determine the maximum temperature obtained in ion beam-heated targets.

It should also be noted that in making a direct comparison with experimental spectra the spatial profile of the beam on the target should be taken into account [9]. For instance, if the beam power density profile in Fig. 2.10 corresponds to the center of the beam, the wings of the beam will have a lower current density, resulting in a portion of the target which is heated to lower temperatures. If this region is seen by the spectrometer, a space-integration of the K_α spectra must be performed. This will result in greater emission from the relatively low ionization stages than is shown in Fig. 2.15.

Absorption spectra for simulation times ranging from $t = 10$ ns to 80 ns are shown in Fig. 2.16. In addition to K_α satellites, K_β lines — which are due to $1s \rightarrow 3p$ transitions — are also observed. (K_β lines are generally not seen in emission because of their much weaker intensity.) At early times only K_β absorption lines are seen. K_α absorption lines require states with vacancies in the $2p$ subshell, which do not become populated until $T \gtrsim 10$ eV. At late times a significant shift to higher ionization stages is seen. Note that to observe these K_α lines in absorption at late time only required the presence of a backlighter. The problems associated with determining the late-time plasma conditions from emission spectra (i.e., weak intensities) do not occur. Thus, absorption spectroscopy may have very significant advantages for determining plasma conditions after the peak of the beam pulse. We also note that absorption spectroscopy may also prove very valuable because of potential uncertainties associated with multiple ionization effects [10,11]. This is especially true for Li beam experiments.

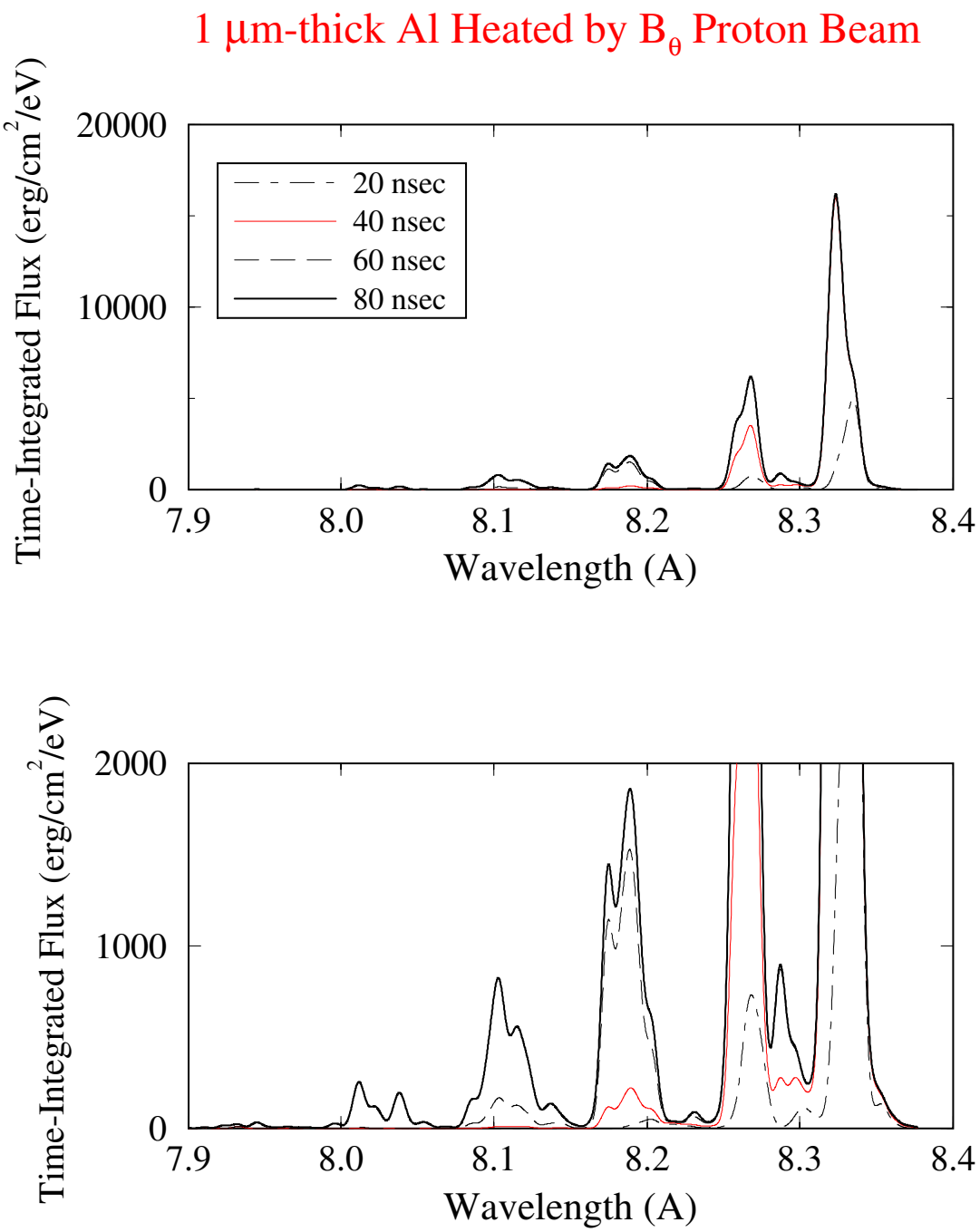

Figure 2.15. Time-integrated K_α satellite emission spectrum for B_θ diode simulation. The bottom plot shows the emission for the higher ionization stages on a finer scale.

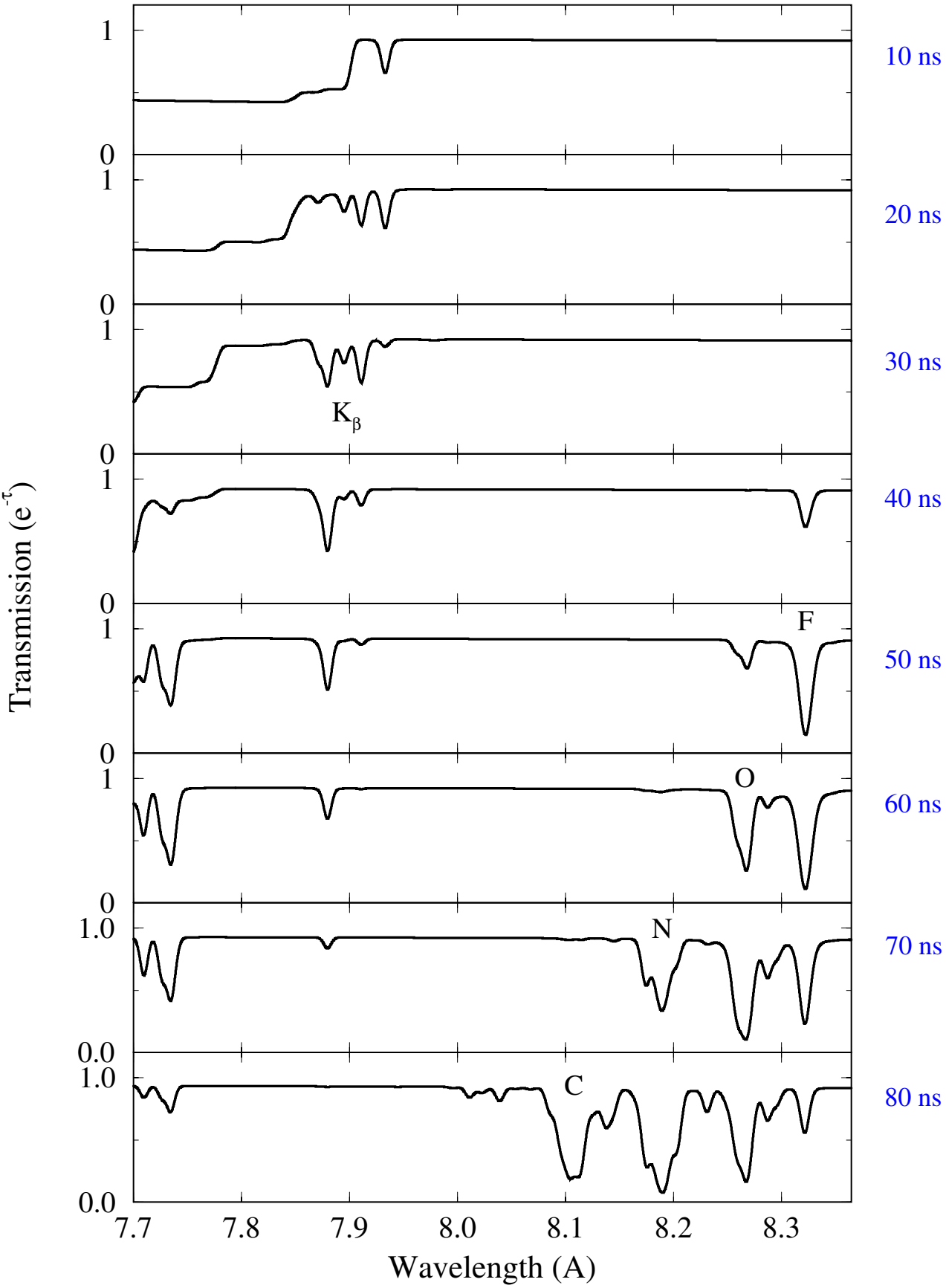

Figure 2.16. Calculated K_α satellite absorption spectra at 10 ns time intervals for the B_θ diode simulation.

2.4. Summary of Radiation-Hydrodynamics and CRE Simulations

The above simulations have been performed to aid in the interpretation of x-ray spectra obtained in initial target heating experiments at FZK. Calculations were performed for both laser-produced plasmas and ion beam-heated plasmas to try to understand why K_α satellites were observed for Al targets, but not Na targets, in B_θ diode experiments. Our calculations suggest that the K_α line intensities from Na and Al targets should be of similar magnitude. In addition, the flux levels predicted from our laser-produced plasma simulations appear to be significantly higher than those deduced from spectroscopic measurements. This suggests that the inferred intensities of Na K-shell lines may be degraded due to some instrumental effect (e.g., a filter, sensitivity, etc.).

Calculations were performed to predict time-integrated Al K_α spectra from KALIF B_θ diode experiments. The simulations predict that the cold K_α feature ($\lambda = 8.34$ Å) should be the most intense, followed by the O-like feature at $\lambda = 8.27$ Å. These results are in qualitative agreement with initial spectroscopic measurements. However, it was noted that to make a direct comparison with experiment, the spatial profile of the proton beam on the target must be considered because the spectrometer sees regions outside of the most intense part of the beam. Our simulations show the difficulties associated with trying to determine the target's *maximum* temperature from emission spectroscopy. Because of the low emission levels, absorption spectroscopy should provide much better constraints on the target plasma conditions at late times.

3. A Unified Self-Consistent Field Model for Calculating Ion Stopping Powers in Plasmas

3.1. Introduction

For many years, the stopping of energetic ions in matter has been a subject of great interest. In the context of ion driven inertial confinement fusion (ICF) experments, the stopping power of ions in matter of both solid and plasma states is crucial for target designs. For reliable diagnostics and evaluation of the ion beam and target parameters such as beam intensity, temperature, and density, one must know the stopping power accurately. Several comprehensive reviews of calculations and measurements of ion stopping power in ICF targets have been given by Mehlhorn [7], Deutsch [12], and Peter [13].

For typical plasma conditions in ion beam-target interaction experiments, the target plasmas are often only partially ionized. Both bound and free electrons make contributions to the stopping power. A most commonly used method for calculating the ion stopping power in partially ionized plasmas is to divide the stopping electrons into two groups: those bound to the plasma ions and those which constitute the plasma free electrons. The number of free electrons in the plasma is determined by solving the Saha equation. The contribution of each group of electrons to the stopping power is calculated separately. For example, most of the stopping power calculations [14] use the Bethe equation [15] for the bound electrons and use a separate term for the plasma free electrons. Although this kind of combined stopping power model has provided a reasonable description of the energy deposition of both light and heavy ions in ICF plasmas, a weakness of it is that the assumption of the definite separation of "bound" and "free" electrons may not be appropriate for high density ICF plsamas. If we represent the effect of the plasma by a fluctuating microfield, the pertubations of it can cause an orbital electron to have some nonzero probability of becoming unbound from its original nucleus. However, an electron which is unbound in a one-center system may still be bound in a two-center system consisting of the original nucleus and a neighboring ion. Moreover, the electron may also be bound in a 3,4,..., center system which includes additional neighboring ions. A relevant discussion of these quasi-free electrons has been given by More [16], who makes use of the formal collision theory to describe these electrons within the framework of the ion sphere atomic model. Since the characteristic interaction velocities of 'bound' and 'free' electrons are different in ion stopping, the 'quasi-bound' electrons play the role of bridging them. The effects of 'quasi-bound' electrons on stopping power have not been studied in detail before. Another drawback of the combined stopping power model is that it uses different models for different

energy regimes, and the separation boundary of 'low' and 'high' energy regimes is somewhat ambiguous.

In 1963 the first unified approach to ion stopping and range theory was made by Lindhard, Scharff and Schiott [17] and their approach is commonly called the LSS-model. This work brought together Lindhard's elegant dielectric formulation of stopping theory and local density approximation, and bridging approximations were made so that calculations of stopping power of cold material could, for the first time, be made within a single model. However, since the LSS-model is based on Thomas-Fermi statistical atoms, it naturally shows no shell effects and is only accurate for atoms with many electrons in the intermediate range where they are neither fully stripped nor almost neutral. With the LSS-model it is possible to predict the ion stopping power of solids within a factor of 2. Later on, significant improvement [18] was made with the incorporation of more realistic Hartree-Fock atoms into the LSS-model. Now, a natural question should be asked is how should we extend the LSS-model to form a single unified model that is capable of accurately predicting the ion range and energy deposition profile as a function of material composition, density, temperature, and degree of material ionization for a variety of different ionic species and beam energies?

In this work we develop a unified self-consistent-field model for ion energy deposition in ion-driven inertial confinement fusion targets. As a starting point, we noticed while looking through many calculations of cold material stopping power in the framework of the LSS-model that the overall accuracy is much better when the solid state Hartree-Fock electron density distribution is used instead of the isolated Hartree-Fock atomic model. On the other hand, Lindhard's stopping power formalism needed to be extended to include finite temperature effects. Hence the present work is concerned with establishing two main points.

The first main point is how to choose an atomic model which is appropriate for the conditions revalant to the ion-driven inertial confinement fusion targets. The requirement for the model is that it should recover the electron density distributions of both solid-state and isolated atom Hartree-Fock models in the corresponding conditions. In 1979 Liberman [19] developed a self-consistent-field "muffin-tin" atomic model for high density plasmas. This model has much of the simplicity of an isolated atom but captures much of the physics of the band-structure model. It provides a self-consistent treatment for both "bound" and "free" electrons in a wide range of plasma conditions. We will use this atomic model to determine the electron density distribution function. Since we are interested in both low-Z and high-Z materials, the relativistic formulation is used. The second main point of this

work concerns the stopping characteristics of the ICF relevant hot plasmas with an electron temperature comparable or smaller than the Fermi one. In this aspect, we take advantage of the full Random Phase Approximation (RPA) dielectric function developed by Maynard and Deutsch [20].

In Section 3.2 we review the Lindhard stopping power formalism and the local density approximation which form a framework of this work. In the Section 3.3 we describe Liberman's "muffin-tin" atomic model and electron distribution function. And in Section 3.4 we discuss the full R.P.A. stopping interaction function. Numerical calculation results and discussion are presented in Section 3.5. An analytic fitting procedure which provides analytic expressions of stopping power for using in hydrodynamic simulations is presented in Section 3.6. Finally, a summary of the work is given in Section 3.7.

3.2. Lindhard's Formalism of Stopping Power and Local Density Approximation

For an ion of charge Ze moving with velocity V in a medium of uniform density ρ, the energy loss due to electron excitation can be conveniently written in the form

$$-\frac{dE}{dx} = \frac{4\pi}{m}\left(\frac{Ze^2}{V}\right)\rho L(\rho, v) \tag{3.1}$$

where L is the stopping number and m is the mass of electron. In the dielectric formalism, L is written as

$$L = \frac{i}{\pi\omega_0^2}\int_0^\infty \frac{dk}{k}\int_{kv}^{kv} \omega d\omega[\varepsilon^{-1}(k,\omega) - 1] \tag{3.2}$$

where ω_0 is the plasma frequency, i.e.,

$$\omega_0^2 = \frac{4\pi e^2\rho}{m} \tag{3.3}$$

and $\varepsilon(k,\omega)$ is the wave number and frequency dependent longitudinal dielectric constant.

Lindhard's formalism to the interaction of a charged particle with a free electron gas makes the following assumptions:

- The free electron gas consists of electrons at zero temperature (single electrons are described by plane wave) on a fixed uniform positive background with overall charge neutrality.
- The initial electron gas is of constant density.
- The interaction of the charged particle is a perturbation on the electron gas.

- All particles are non-relativistic.

With these assumptions, Lindhard obtained the stopping number, L, as

$$L = \frac{6}{\pi} \int_0^{V/VF} u du \int_0^{\infty} dz \, \frac{z^3 f_2(u,z)}{[z^2 + \chi^2 f_1(u,z)]^2 + [\chi^2 F_2(u,z)]^2} \tag{3.4}$$

where

$$\begin{aligned} f_1(u,z) = \frac{1}{2} \quad &+ \quad \frac{1}{8z}\left[1-(z-u)^2\right] \left| \ln \frac{z-u+1}{z-u-1} \right| \\ &+ \quad \frac{1}{8z}\left[1-(z+u)^2\right] \left| \ln \frac{z+u+1}{z+u-1} \right| \end{aligned} \tag{3.5}$$

and

$$f_2(u,z) = \begin{cases} \frac{1}{2}\pi u & for \quad z+u<1 \\ (\frac{\pi}{8z})[1-(z-u)^2] & for \quad |z-u|<1<z+u \\ 0 & for \quad |z-u|>1\,. \end{cases} \tag{3.6}$$

z and u are the reduced wave number and frequency:

$$z = \frac{k}{2k_F} \qquad \text{and} \qquad u = \frac{\omega}{kV_F} \tag{3.7}$$

with k_F and V_F denoting Fermi wave number and velocity

$$E_F = \frac{1}{2} m V_F^2 \equiv \frac{h^2 k_F^2}{2m} = \frac{h^2}{2m} (3\pi^2 \rho)^{2/3}\,. \tag{3.8}$$

The dimensionless quantity χ^2 is defined by

$$\chi^2 = \frac{V_0}{\pi V_F} \tag{3.9}$$

with $V_0 = e^2/\bar{h}$ denoting the Bohr velocity. Some typical illustrations of the variation in Lindhard's stopping number with electron density and energy are presented in Fig. 3.1.

The Lindhard stopping power formalism is a many-body self-consistent treatment of an electron gas responding to a perturbation by a charged particle. It naturally includes the polarization of the electrons by the charged particle and the resultant charge-screening and the plasma density fluctuations. It smoothly treats both individual electron excitation and collective plasmon excitations without separate 'distant' and 'close' collision processes. However, Eq. (3.1) is only vaild for an uniform free electron gas. For a partially ionized plasma, the electron density distribution is no longer uniform because of the presence of

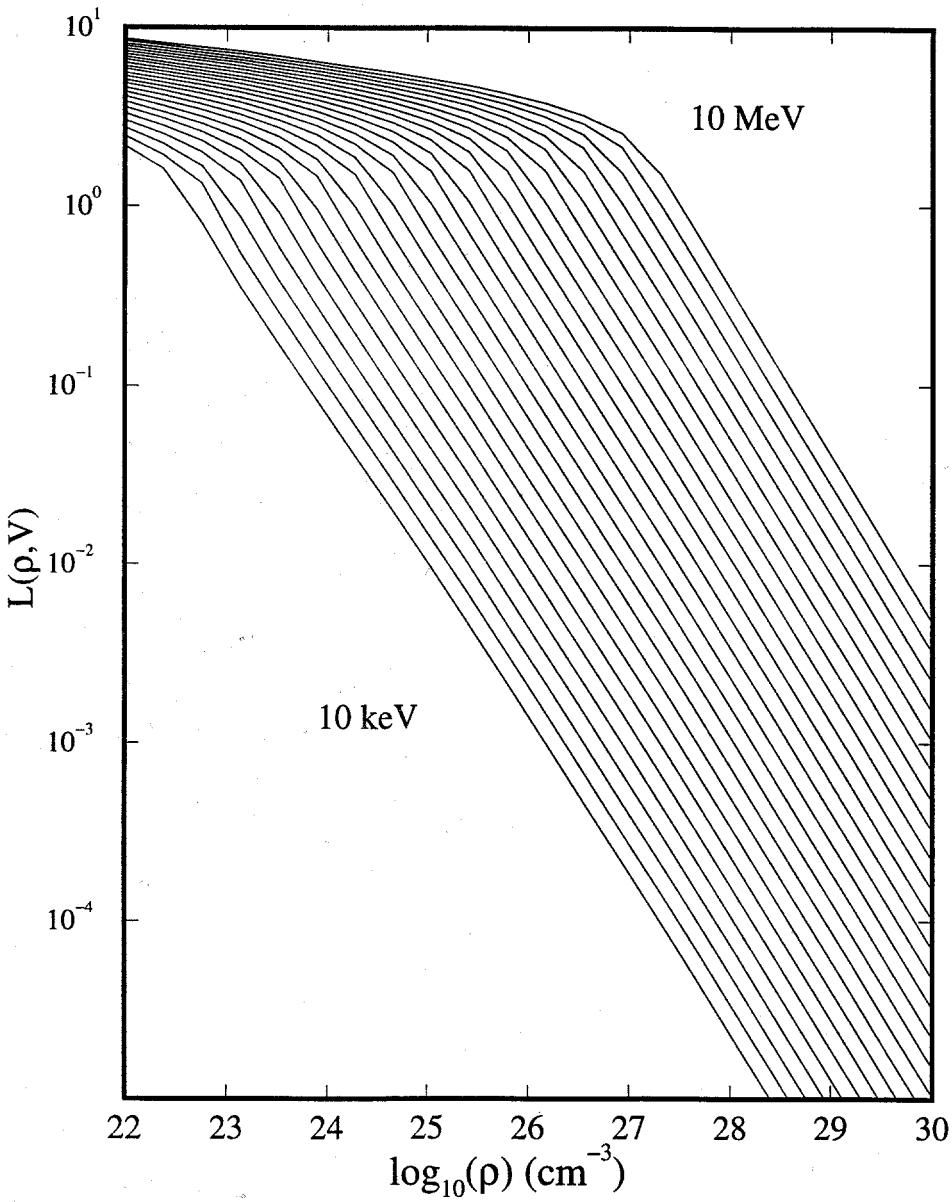

Figure 3.1. Variation in Lindhard stopping number with electron density for selected projectile energies.

bound electrons. In such cases, the Lindhard stopping power formalism can still be directly applied with the use of the local-density approximation [21].

In the local-density approximation, the nonuniform electron cloud is divided into small independent volume elements, and the electron density distribution in each volume element is assumed to be uniform. The stopping power is calculated for a charged particle in a free electron gas of each volume element's density, and the final stopping power is computed by averaging over these values, weighted by their distribution in the nonuniform electron cloud

$$\left(-\frac{dE}{dx}\right) = \frac{4\pi}{m}\left(\frac{Ze^2}{V}\right)^2 \int_0^\infty \rho(r)L(\rho,v)4\pi r^2 dr \tag{3.10}$$

where $\rho(r)$ is the spherically averaged electron density of the target atom.

It can be seen from Eq. (3.10) that the electronic stopping of an ion in a plasma is determined by two key functions, the electron density distribution function $\rho(r)$ and stopping number L.

3.3. Atomic Model And Electron Density Distribution Function

The electron density distribution of an atom is affected by its surrounding environment. This is particularly the case for the outer shell electrons. Figure 3.2 demonstrates the difference between the calculated electron distribution for an isolated atom (denoted HFS for Hartree-Fock-Slater) and that of the same atom in a solid-state lattice [22]. It can be seen that there is a pronounced difference in the spatial variation of the solid-state and isolated atomic electron densities away from the interior of the target atom due to solid-state bonding effects. It was found [23] that this spatial variation in electron density gives rise to a marked change in density-averaged stopping number. Therefore, it is necessary to use solid-state electron densities in the calculation of stopping power of solids.

What should be the appropriate electron density distribution function in stopping power calculations for a plasma atom? To date, the isolated atom model has been most commonly used in the calculations of ion stopping power of plasmas. However, just as for solids, its applicability to hot dense ICF plasmas is questionable [24] because of the marked perturbation of surrounding environment. In order to account for environmental effects on electron distribution properly, we choose a self-consistent-field 'muffin-tin' atomic model [19] in our stopping power calculations. One important feature of this model is that it smoothly connects the solid-state self-consistent-field atomic model and the isolated atom Hartree-Fock model. It naturally extends the solid-state Hartree-Fock model into finite temperature high density plasams. On the other hand, at the low density regime

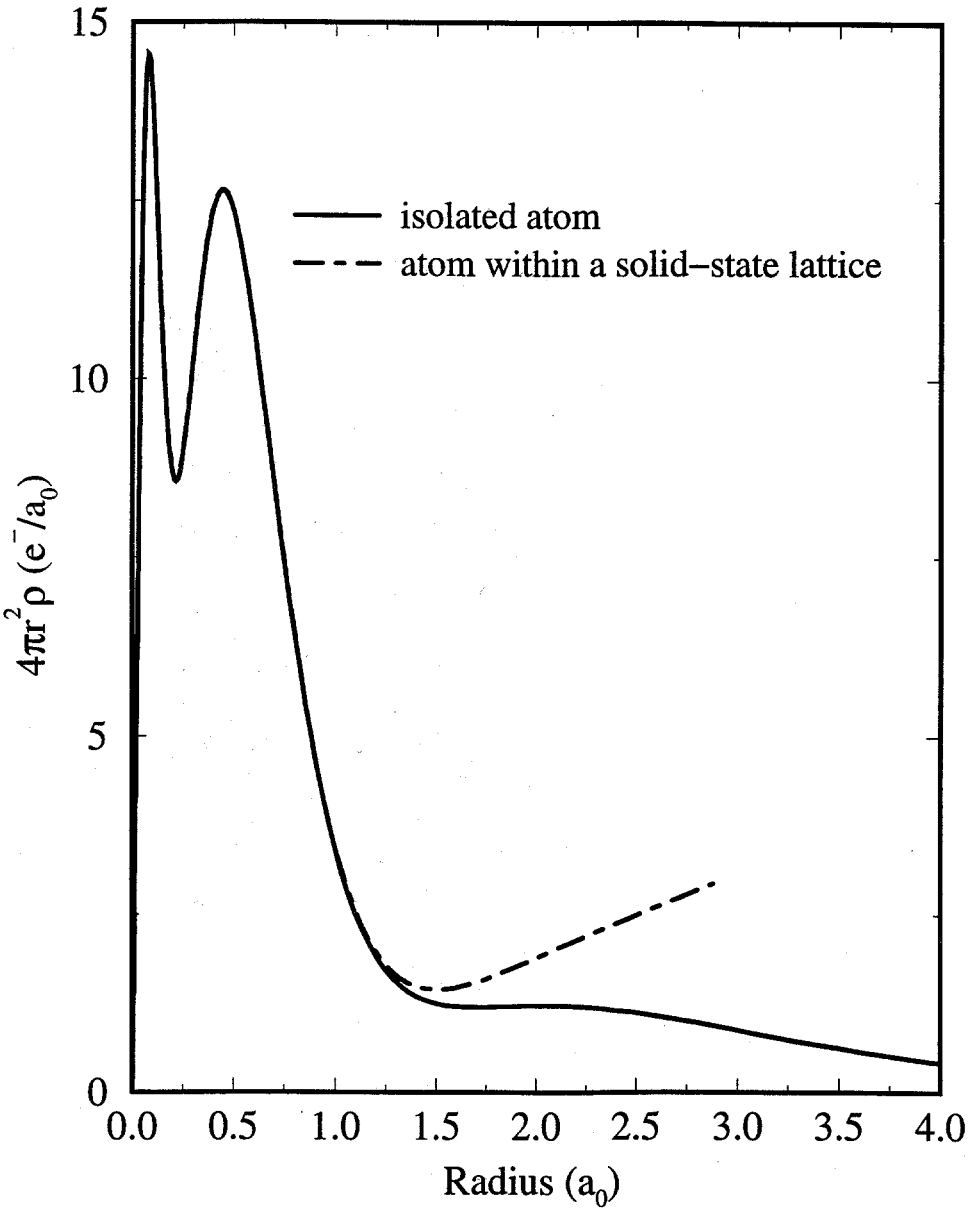

Figure 3.2. Radial electron density profiles for neutral aluminum atoms. Results for isolated atoms and atoms within a solid-state lattice are shown.

it describes an isolated atom or an ion in equilibrium with an electron gas. Therefore, problems of a wide range of temperatures and densities can be accommodated within an unique atomic model.

Figure 3.3 illustrates the model [19]. At the center of a spherical cavity is a point nucleus, outside the cavity there is a uniform distribuition of positive charge which takes the place of the surrounding ions. There are sufficient electrons in the system to give overall electrical neutrality, and the additional requirement of electrical neutrality inside the sphere is imposed. A "muffin-tin" approximation is used for the electron density outside the sphere. The electrons are governed by a set of self-consistent-field one-electron Dirac equations,

$$[c\vec{\alpha}\cdot\vec{\rho}+\beta c^2-c^2+V(r)]\,\phi_i(\vec{r})=\epsilon_i\phi_i(\vec{r}) \tag{3.11}$$

where the potential function is

$$V(r)=\begin{cases} -\frac{Z}{r}+\int_{r'<R}\frac{\rho(r')}{|\vec{r}-\vec{r}'|}-\frac{[3\pi^2\rho(r)]^{1/3}}{\pi}-\nu & \text{for} \quad r<R \\ -\frac{(3\pi^2\bar{\rho})^{1/3}}{\pi} & \text{for} \quad r>R\,. \end{cases} \tag{3.12}$$

R is the radius of the cavity which is electrically neutral, and is determined by the conditions of the plasma. The Lagrangian multiplier ν is given by

$$\nu=\left\{\left[4-\frac{\bar{\rho}}{\rho(R)}\right](3\pi^2\bar{\rho})^{1/3}-3[3\pi^2\rho(R)]^{1/3}\right\}/4\pi\,. \tag{3.13}$$

The electron density itself is given in terms of normalized one electron orbital functions and "muffin-tin" approximation

$$\rho(r)=\begin{cases} \frac{\int\rho_-(\vec{r})\sin\theta\,d\theta\,d\varphi}{4\pi} & r<R \\ \frac{\int_{x>R}\rho_-(\vec{x})\,d\vec{x}}{\int_{x>R}d\vec{x}}=\bar{\rho} & r>R \end{cases} \tag{3.14}$$

$$\rho_-(\vec{r})=\sum_i\eta_i\,|n_i(\vec{r})|^2$$

and the orbital occupation number is determined by the Fermi-Dirac distribution

$$\eta_i=\frac{1}{\exp\left[\frac{(\epsilon_i-u)}{kT}\right]+1}\,. \tag{3.15}$$

The sum in Eq. (3.15) includes electrons in ground states, excited states, and an integral over the continuum. The continuum states are treated on the same basis as the bound states in this model, and as a result there is a smooth transition from bound state to

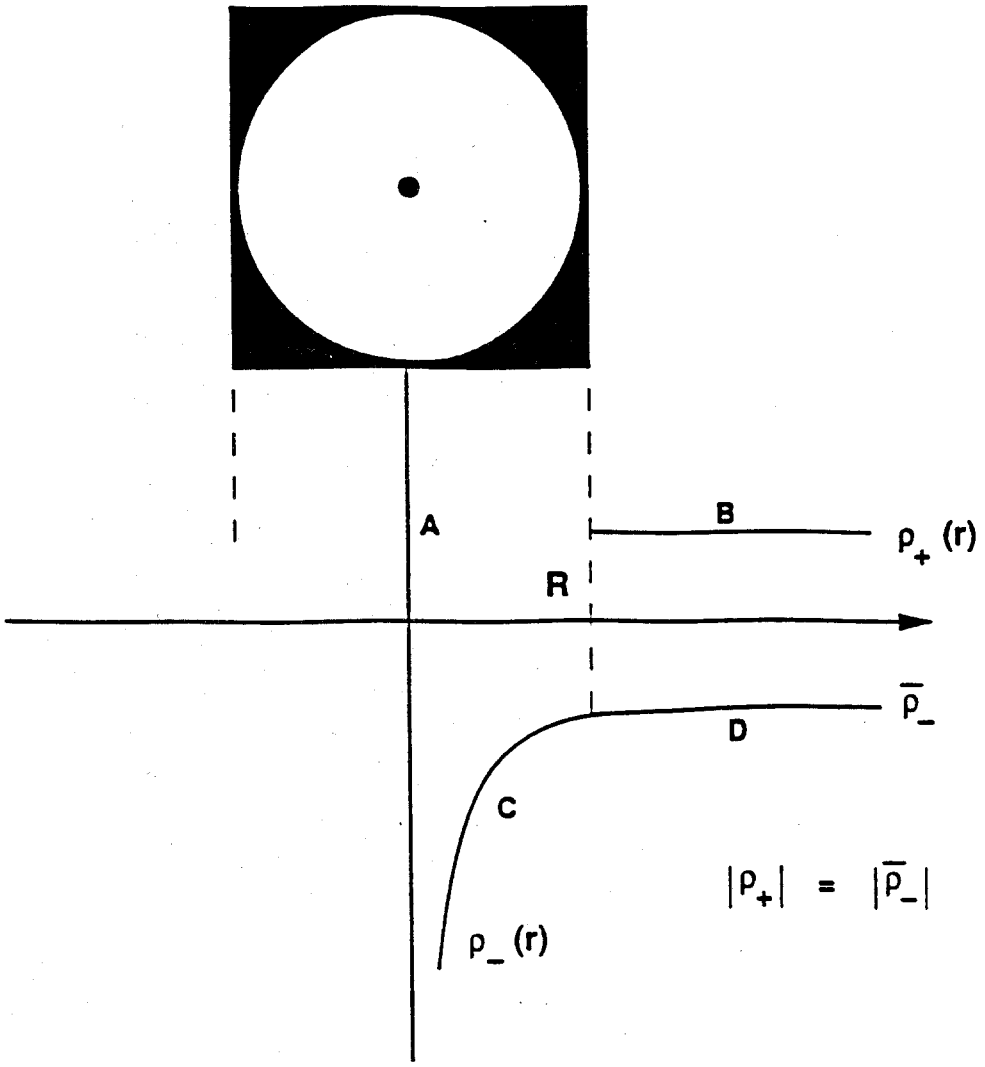

Figure 3.3. A schematic charge distribution for the "muffin-tin" atomic model: (a) a point nucleus at the center of a spherical cavity; (b) a constant positive charge density outside the cavity which represents surrounding ions; (c) a spherically symmetric electronic charge density inside the cavity; (d) a volume average electronic charge density outside the cavity. R is the radius of the cavity.

narrow resonance and then to broad resonance. The implication of this treatment is that there is not a sharp cut in statistical distribution between "bound" and "free" electrons.

The electron density distributions generated by this atomic model are shown in Fig. 3.4 and Fig. 3.5. Fig. 3.4 shows the calculated electron density distribution of a gold atom at normal matter density along with that of the isolated atom Dirac-Fock calculation. It is seen that while the 'muffin-tin' electron density distribution is almost identical to that of an isolated atom for inner-shell electrons, there is a significant difference in the outer shell regime. The temperature effect on electron density distributions is shown in Fig. 3.5. As temperature increases, more and more electrons are excited and ionized. Therefore, we see the electron density decreases in the inner regime and increases in the outer regime. It is important to note that the 'muffin-tin' model provides a self-consistent picture for electrons in all states.

3.4. The Random-Phase-Approximation Stopping Interaction Function

For ICF relavant hot dense plasmas, the standard Lindhard stopping number is no longer valid. In order to extrapolate the zero temperature Lindhard stopping quantity to plsamas at any temperature, Maynard and Deutsch [20] have developed a model which makes use of the full R.P.A. dielectric function to give formulae for the temperature dependent stopping number of electron stopping:

$$L = \frac{6}{n\chi^2} \int_0^{V/V_F} udu \int_0^{\infty} dz \, \frac{z^3 \chi^2 f_2(u,z)}{[z^2 + \chi^2 f_1(u,z)]^2 + [\chi^2 f_2(u,z)]^2} \tag{3.16}$$

where

$$\begin{aligned} f_1(u,z) &= \int_0^{\infty} dk \, n^0(k) + \pi T_e \sum_{n=b}^{\infty} \left\{ \frac{b_n}{\gamma_n} - \frac{1}{4z} \left[\tan^{-1}\left(\frac{P_+ + a_n}{b_n}\right) \right.\right. \\ &+ \left.\left. \tan^{-1}\left(\frac{P_+ - a_n}{b_n}\right) - \tan^{-1}\left(\frac{P_- + a_n}{b_n}\right) - \tan^{-1}\left(\frac{P_- - a_n}{b_n}\right) \right] \right\} \end{aligned} \tag{3.17}$$

$$f_2 = -\frac{\pi T_e}{8z} \ln \left\{ \frac{1 + \exp\left[\frac{\gamma - P_+^2}{Te}\right]}{1 + \exp\left[\frac{\gamma - P_-^2}{Te}\right]} \right\} \tag{3.18}$$

with

$$\begin{aligned} n^0(R) &= \left[\exp\left(\frac{k^2 - \gamma}{T_e}\right) + 1 \right]^{-1} \\ Te &= \frac{T}{T_F} \end{aligned}$$

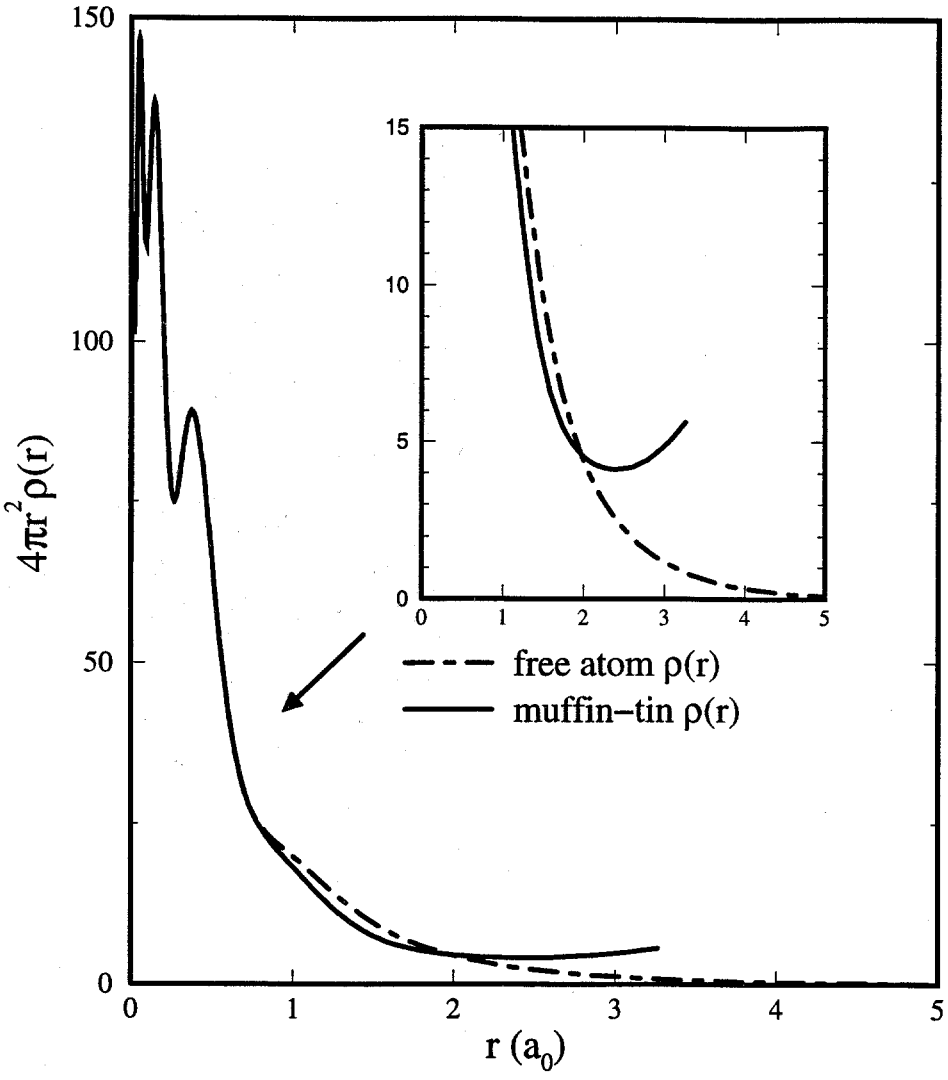

Figure 3.4. Comparison of isolated atom Dirac-Fock radial electron density with that from the muffin-tin model.

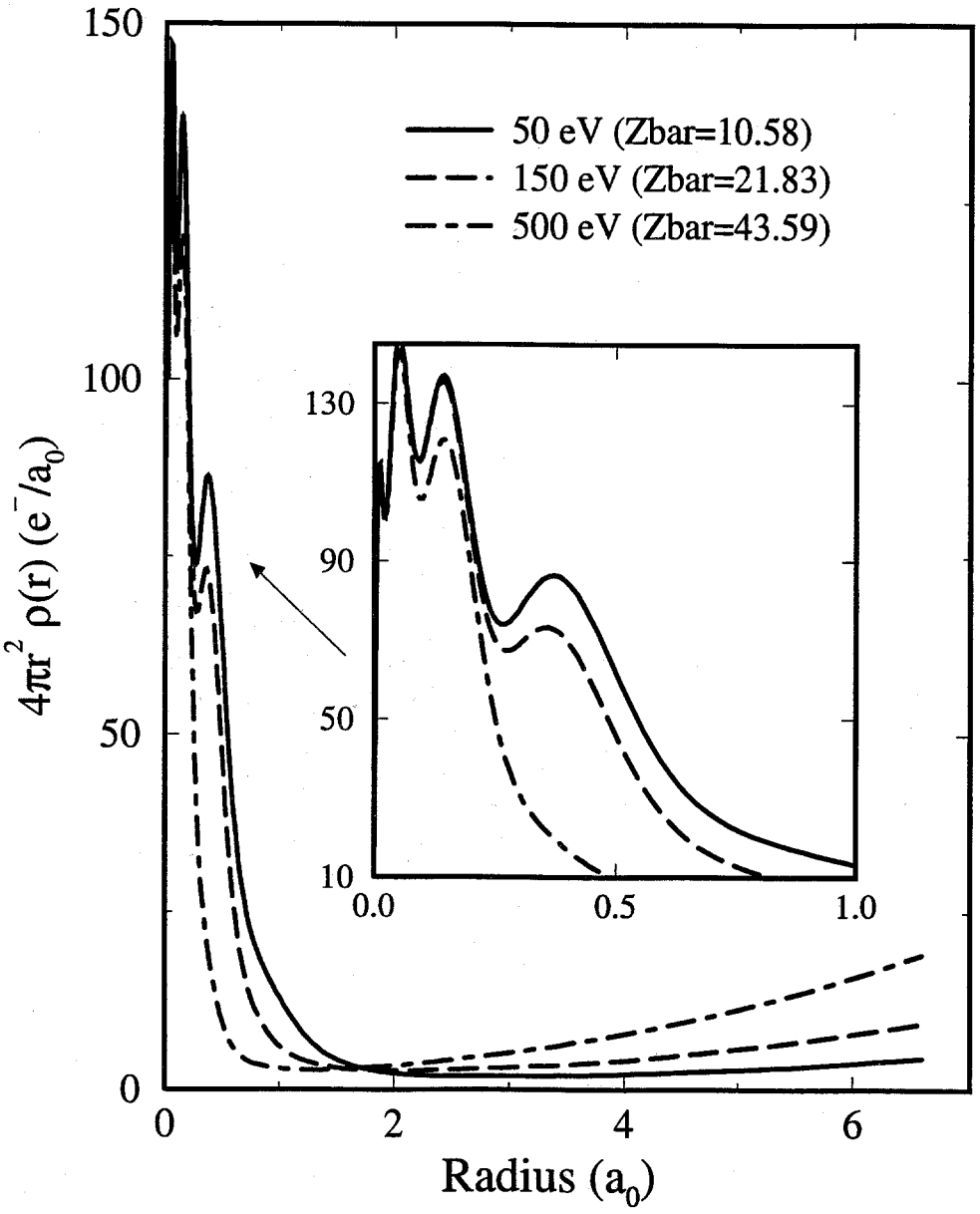

Figure 3.5. Radial electron density profiles for gold at selected temperatures. Results are calculated with the muffin-tin atomic model.

$$
\begin{aligned}
P_{\pm} &= u \pm z \\
\gamma &= \alpha T_e
\end{aligned} \tag{3.19}
$$

and α is determined from

$$
F_{1/2}(\alpha) = \frac{2}{3} T e^{-3/2} \,. \tag{3.20}
$$

The coefficients a_n and b_n are given by

$$
\begin{aligned}
a_n &= \pm \frac{1}{2} \left\{ \gamma + [\gamma^2 + (2n+1)^2 \pi^2 T e^2]^{1/2} \right\}^{1/2} \\
&\text{and} \\
b_n &= \pm \frac{1}{2} \left\{ \gamma + [\gamma^2 + (2n+1)^2 \pi^2 T e^2]^{1/2} \right\}^{1/2} .
\end{aligned} \tag{3.21}
$$

It is important to note that with Eq. (3.17) and (3.18), one can recover the two well-known results at low and high temperature limits [20].

Direct application of RPA stopping number to large scale stopping power calculations is a formidable task since f_1 is a very slowly convergent quantity. We have chosen an interpolation formula of $L(T, V)$ which bridges the accurate asymptotic expression of Eq. (3.16) in both the small and large projectile velocity limits [20]:

$$
L(V_1, T_e) = \begin{cases} L^1 = \left(\frac{V}{V_F}\right)^3 C(\chi^2, \alpha) \, \frac{1}{1+GV^2} & V \le V_{\text{int}} \\ L^2 = \ln\left(\frac{2mV^2}{t\omega_p}\right) - \frac{\langle V_e^2 \rangle}{V^2} - \frac{\langle V_e^4 \rangle}{2\gamma^4} & V \ge V_{\text{int}} \end{cases} \tag{3.22}
$$

where

$$
\left\langle \frac{V^{2n}}{V_F^2} \right\rangle = \frac{T_e^n \, F_{n+1/2}(\alpha)}{F_{1/2}(\alpha)} \tag{3.23}
$$

$$
C(\chi_1^2, \alpha) = \int_0 \infty \frac{dz \, z^3}{\left(z^2 + \chi^2 \int_1 (z, 0)\right)^2 \left[1 + \exp\left(\frac{z^2 - \alpha}{Te}\right)\right]} \tag{3.24}
$$

and G is fixed by $L^1(V_{int}) = L^2(V_{int})$. Detailed numerical calculations have shown that the relative error of this interpolation formula is smaller than a few percent at any temperature.

In order to demonstrate the sensitivty of stopping number on temperature, we have calculated RPA stopping numbers for ions of various energies stopped in a uniform electron gas with density of 10^{23} cm^{-3}. The calculated results are shown in Fig. 3.6. We see that for slow ions, the stopping number is very sensitive to the temperature, while for fast ions the temperature effect is negligible.

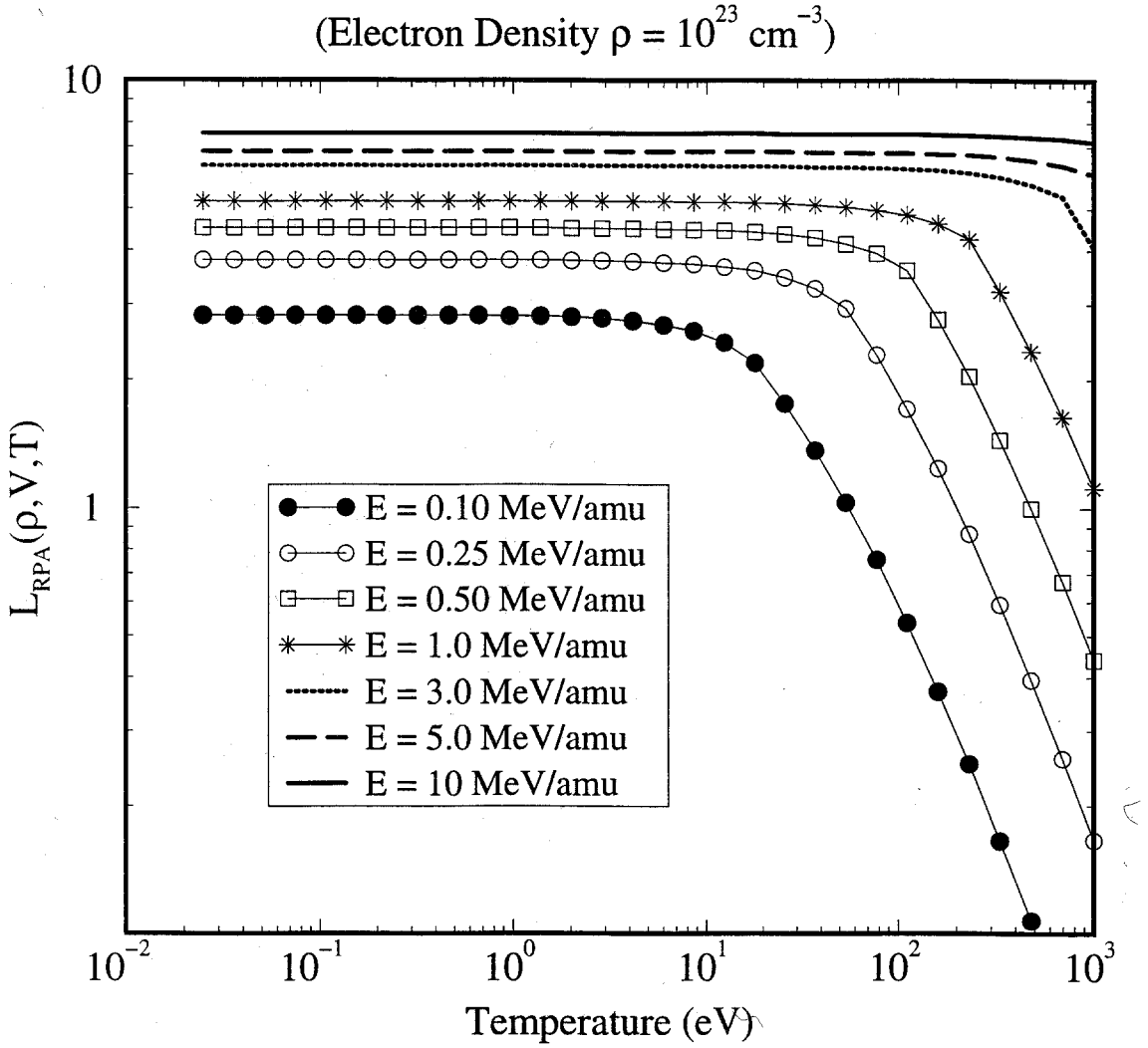

Figure 3.6. Variation in RPA stopping number with temperature for selected projectile energies.

3.5. Numerical Results

The stopping of proton on cold aluminum has been well studied. We begin by studying the case of a monoenergetic beam of proton ions incident on a planar aluminum target so that we can check the validity of charge density distribution represented by the 'muffin-tin' atomic model. Figure 3.7 shows the related change in the calculated proton stopping power in neutral aluminum as compared to experimental data using isolated atom HFS electron distribution and 'muffin-tin' electron distribution discussed above. It can seen that while in the high energy regime both atomic models give good agreement with the experimental data, the low energy stopping power is over-predicted for isolated atoms. It has been known that the low energy ion and high energy ion are mainly stopped by two different parts of electrons of the target atom. Most of the energy of the low energy ion is lost to outer shell electrons, while the inner shell electrons play a major role in stopping high energy ions. As mentioned above, while outer shell electrons are strongly affected by the surrounding environment, inner shell electron distribution is relatively stable. Significant difference is seen in the spatial variation of the 'muffin-tin' electron densities and isolated atom HFS electron densities away from the interior of the target atom due to solid state bonding effects. For inner shell electrons, especially for K-shell electrons, density distributions of two models are almost identical. The good overall agreement of the calculated stopping power with the experimental data demonstrates that the electron distribution of the 'muffin-tin' atomic model is quite accurate for both outer and inner shell electrons.

In Figure 3.8 the calculated proton stopping power on a cold gold target with two different atomic electron densities is shown together with the experimental data [25]. We see that for this high Z target, the calculated stopping power with the 'muffin-tin' electron density shows good overall agreement with the experimental data.

Figure 3.9 shows the stopping power of a monoenergetic beam of carbon ions incident on a planar gold target. Our calculated result is compared with Northcliffe's tabulated data [26] and the results of two other different models [7]. It can be seen that the Bethe model is only valid for the high energy range, while the LSS model is accurate in the low energy range. Our result agree well with the tabulated data over the whole energy range.

Figures 3.10 and 3.11 show the stopping powers for protons in hot gold plasmas. Figure 3.10 represents the case of a gold target having $T_e = 1$ keV, $\rho = 0.193$ g/cm^3, and Figure 3.11 considers the case of a gold target having $T_e = 50$ eV, $\rho = 1.93$ g/cm^3. In the first case, there are about 270 electrons/Debye sphere, while in the second case, this number is only about 2.5. In both cases there is fairly good agreement between our

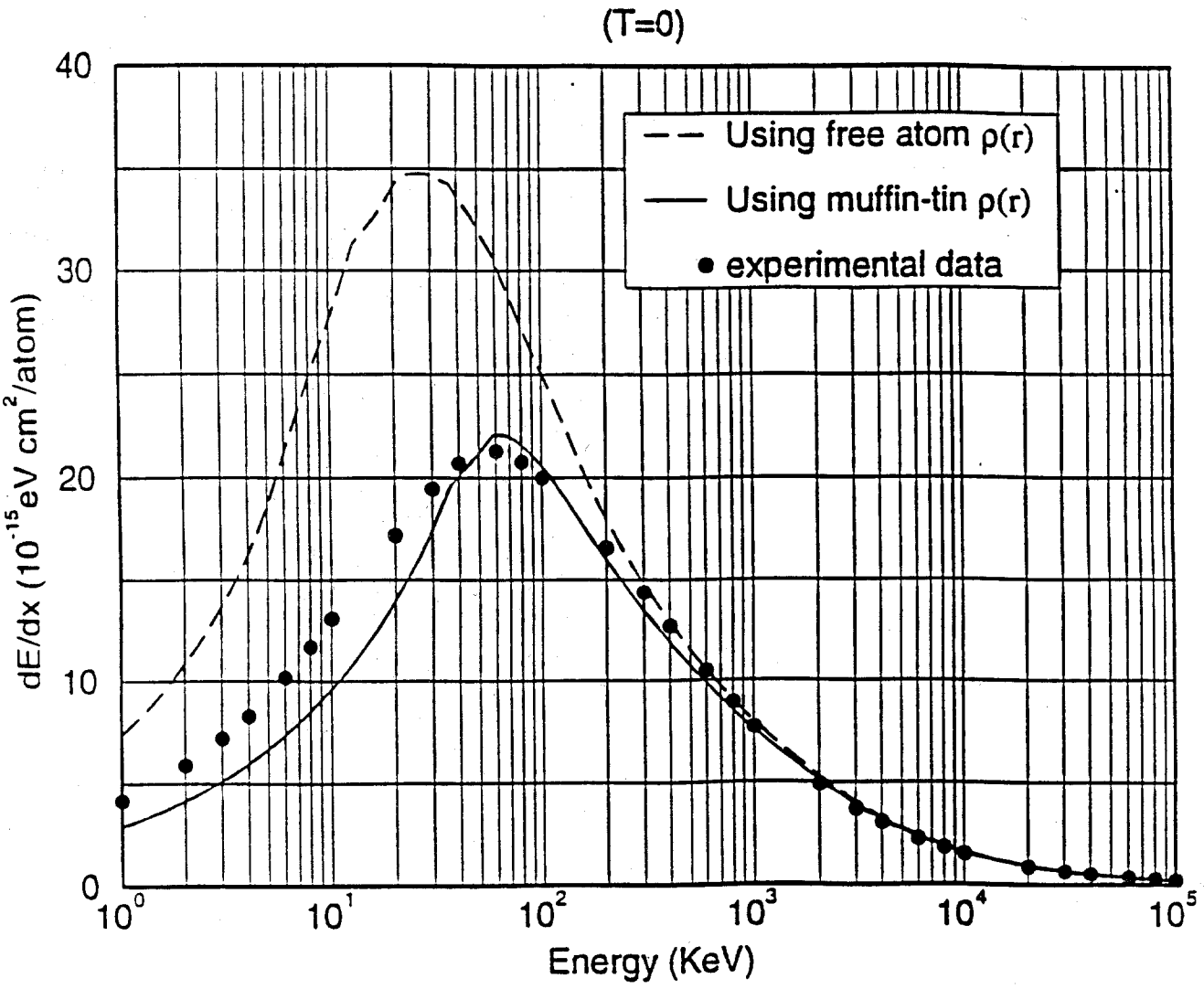

Figure 3.7. Comparison of proton stopping power in neutral aluminum as a function of energy.

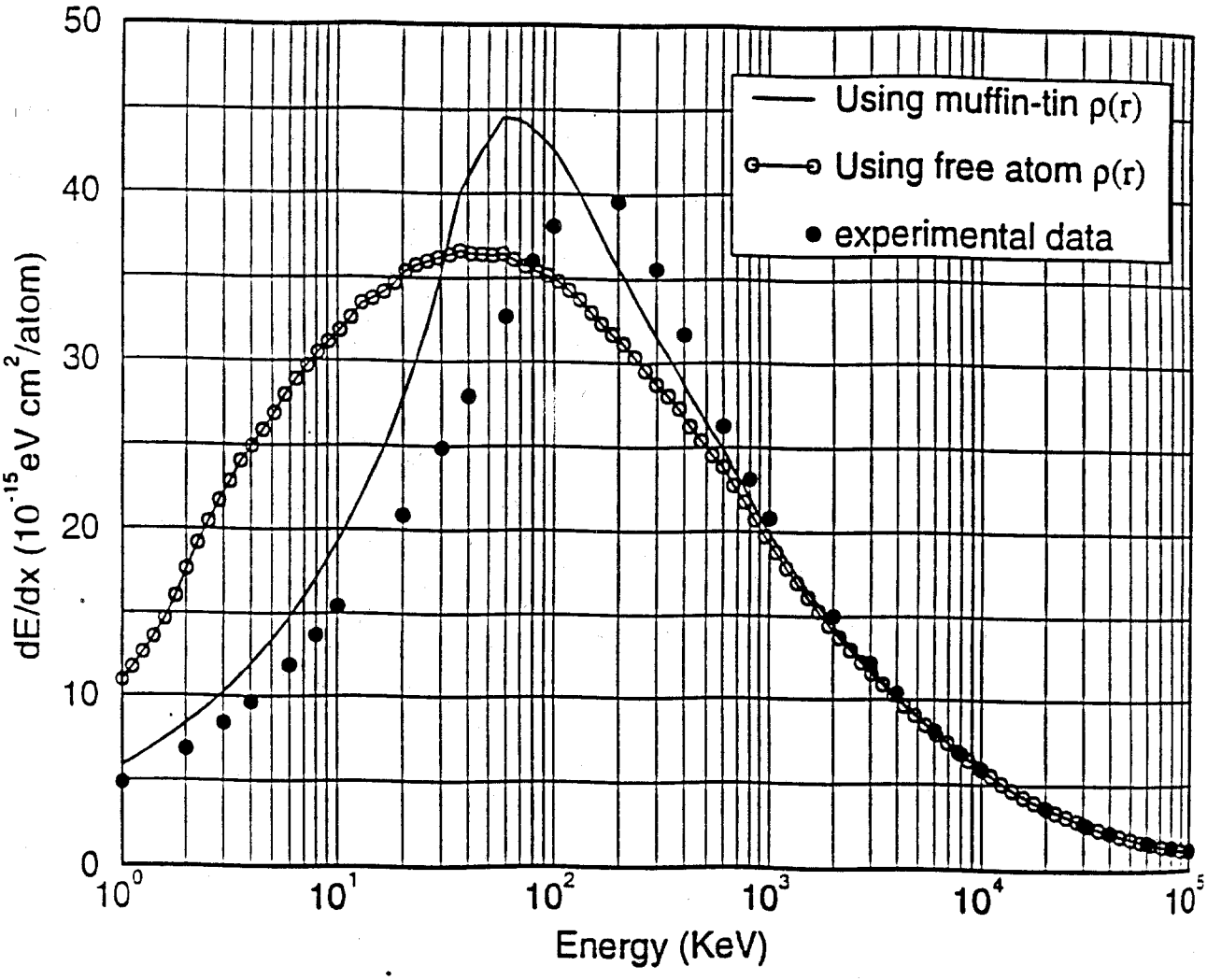

Figure 3.8. Comparison of proton stopping power in neutral gold as a function of energy.

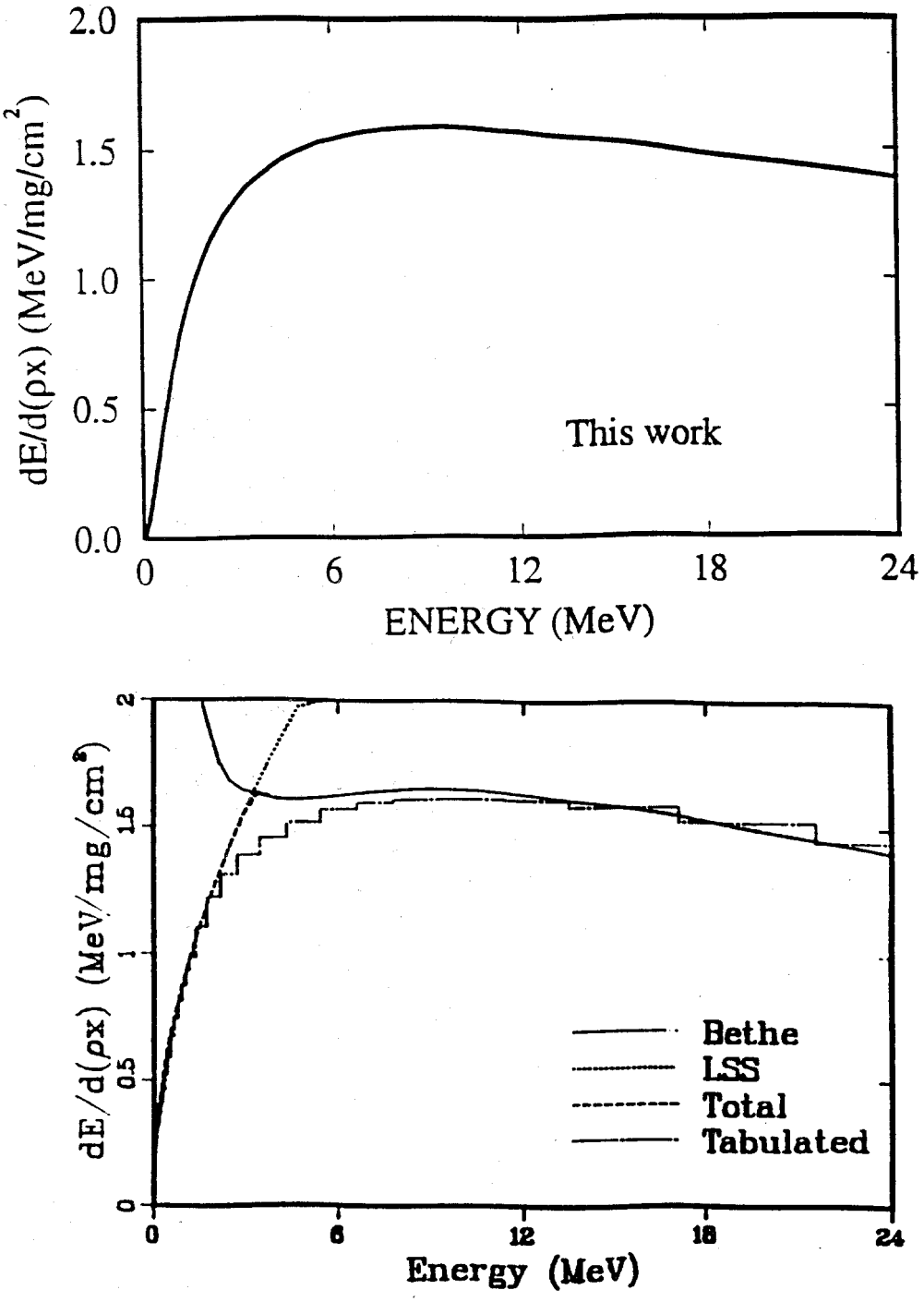

Figure 3.9. Stopping power of solid density room temperature gold for carbon ions. Shown are the stopping powers predicted by several different models.

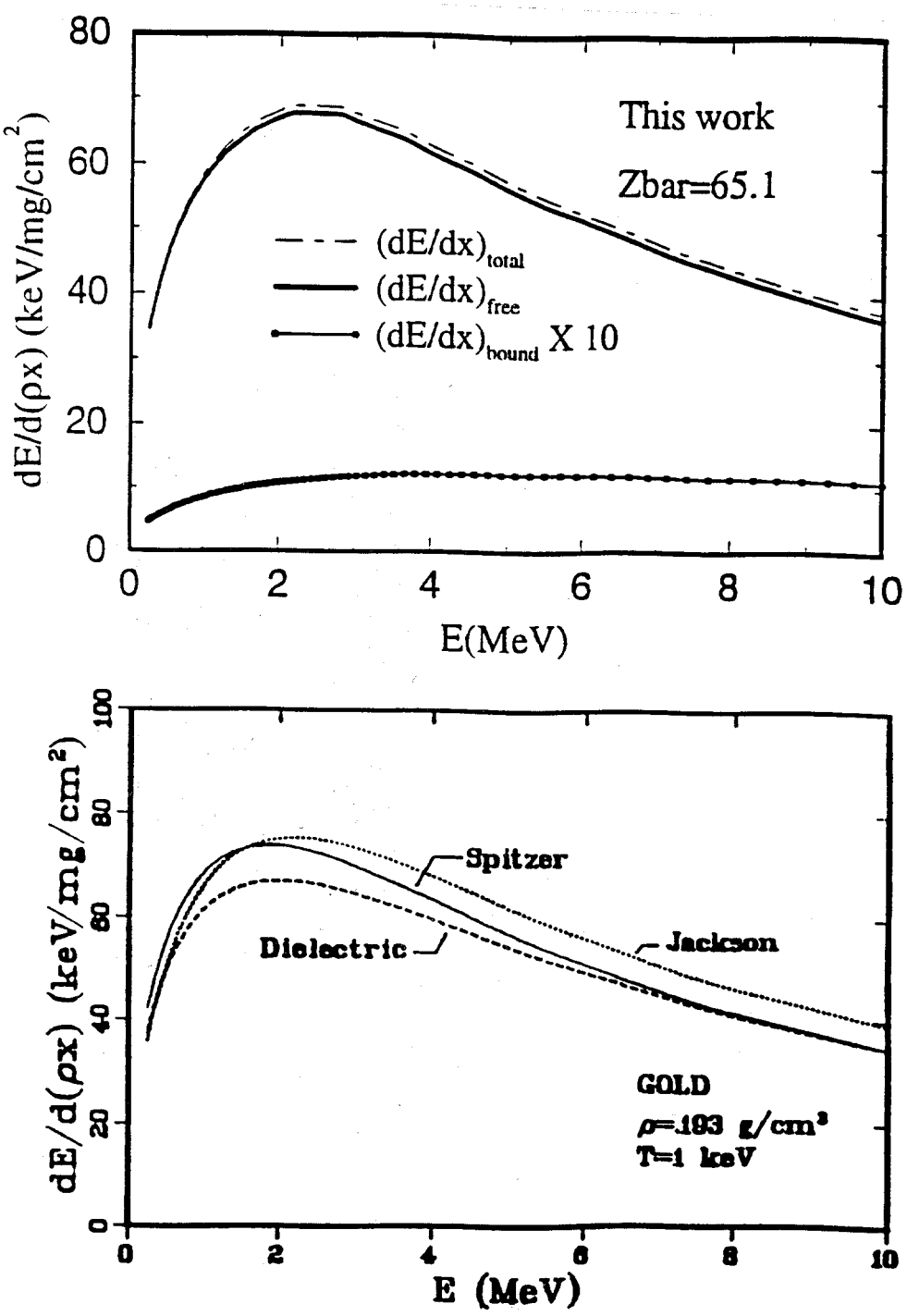

Figure 3.10. Stopping power for protons in a gold plasma having $T_e = 1$ keV, $\rho = 0.193$ g/cm^3.

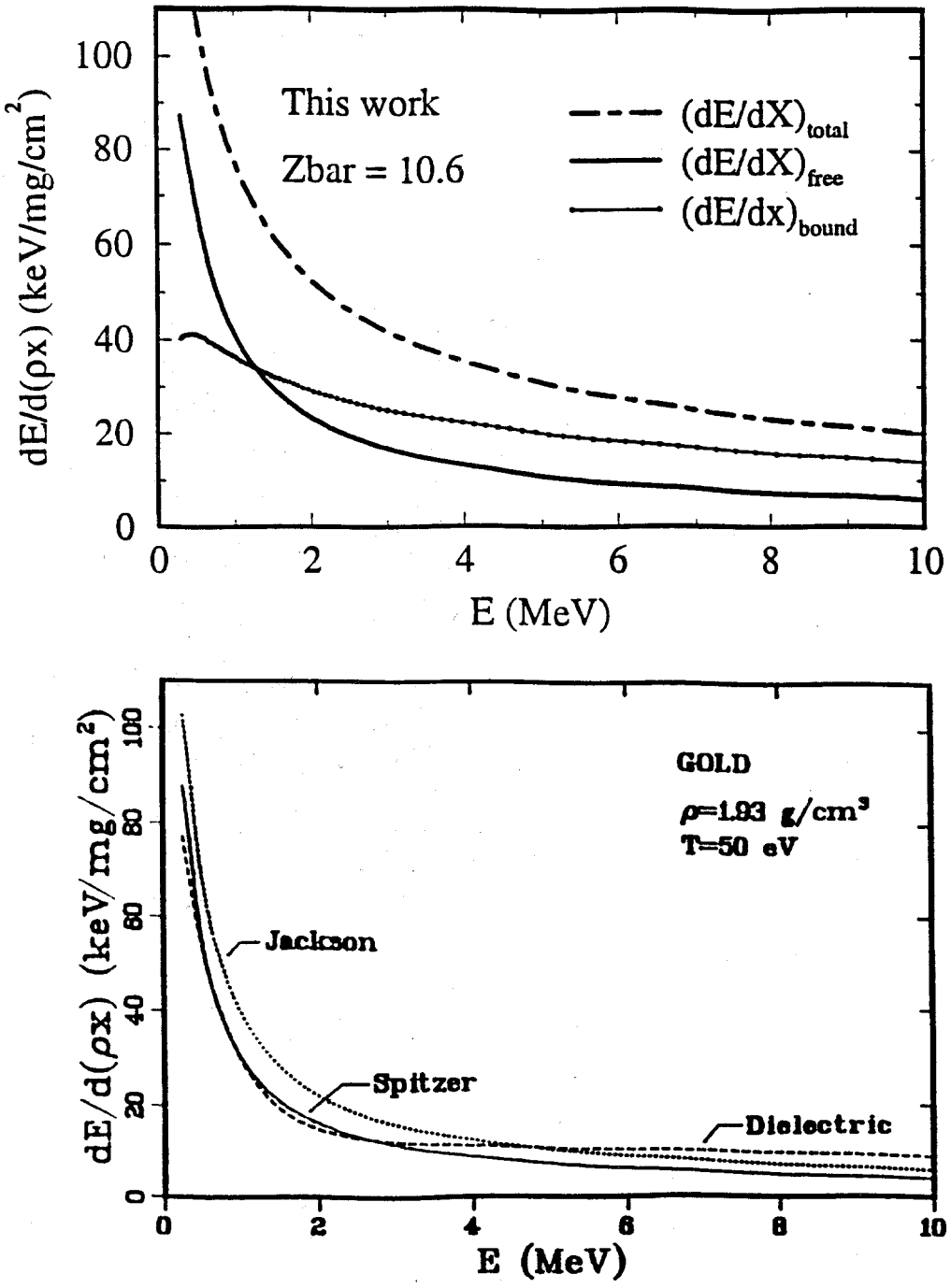

Figure 3.11. Stopping power for protons in a gold plasma having $T_e = 50$ eV, $\rho = 1.93$ g/cm^3.

result and that of three other commonly used models. These two cases correspond to two completely different plasma conditions. The first case represents a weakly coupling plasma, while the second case is a strongly coupling case. The good agreement of our results with the results of other commonly used models indicates that our stopping model is valid for a wide range of target conditions.

Finally, we come to the main point of this work: studying the ion stopping characteristics of hot targets with the use of a self-consistent treatment for both bound and free electrons. In this regard, we have calculated the proton range in a hot gold target with the model discussed in previous sections and made comparisons with the results of the Generalized Oscillator Strength (GOS) model [27] and that of the scaled-Bethe model [24]. Figures 3.12 and 3.13 demostrate the variation of the range in gold with ionization for protons of various energies. Results of this work, GOS results and those using the scaled-Bethe model are shown. There are two points of interest in this comparison. First of all, the range is predicted to decrease more slowly with ionization for GOS results. Our results lie somewhere between GOS results and scaled-Bethe results. Secondly, our results show a smooth decrease with ionization in all the cases, while the GOS model predicts that the range for high energy projectiles can initially increase with ionization of the atom.

It has been argued [24] that such an initial range lengthening characteristic in high Z targets can be interpreted in terms of the difference in the interaction velocities of the target electrons when they are in their bound and free states. It should be noted that the key point of this interpretation is that there is a sharp cut between the bound and free electrons, the characteristic velocity of a bound electron is given by the local Fermi velocity and the characteristic velocity of free electron is the thermal velocity. However, this is not the case in reality. On the other hand, the GOS model neglects the contributions from bound electrons in excited states. These excited electrons are less bounded than those in the subshells of the ground configuration, and their characteristic velocities should be somewhere between the local Fermi velocity and thermal velocity. If the stopping effect from excited electrons is included in the GOS calculation, we expect that the initial range lengthening features in the GOS results could be removed. This needs to be verified in future investigations. In our calculations, contributions from electrons in all states (ground, excited, and continuum states) are essentially taken into account in a self-consistent manner. This characteristic of the model is reflected in Eq. (3.15). The sum in Eq. (3.15) runs through the ground state and all excited states and continuum states. The population of each state is determined by the Fermi-Dirac distribution. The difference between our results and the GOS results demonstrates that the contributions

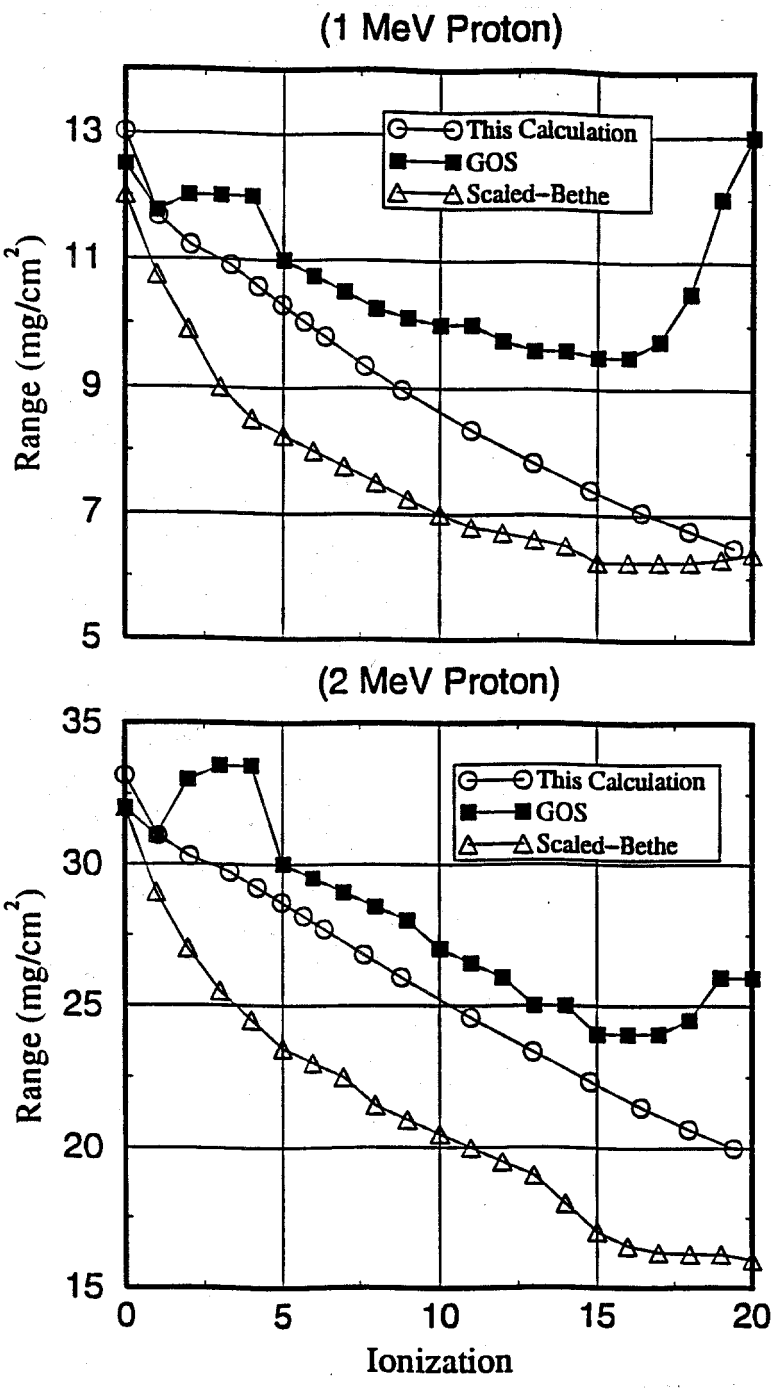

Figure 3.12. Stopping range of 1 MeV and 2 MeV protons in gold as a function of ionization state of the target. Results predicted by three different models are presented.

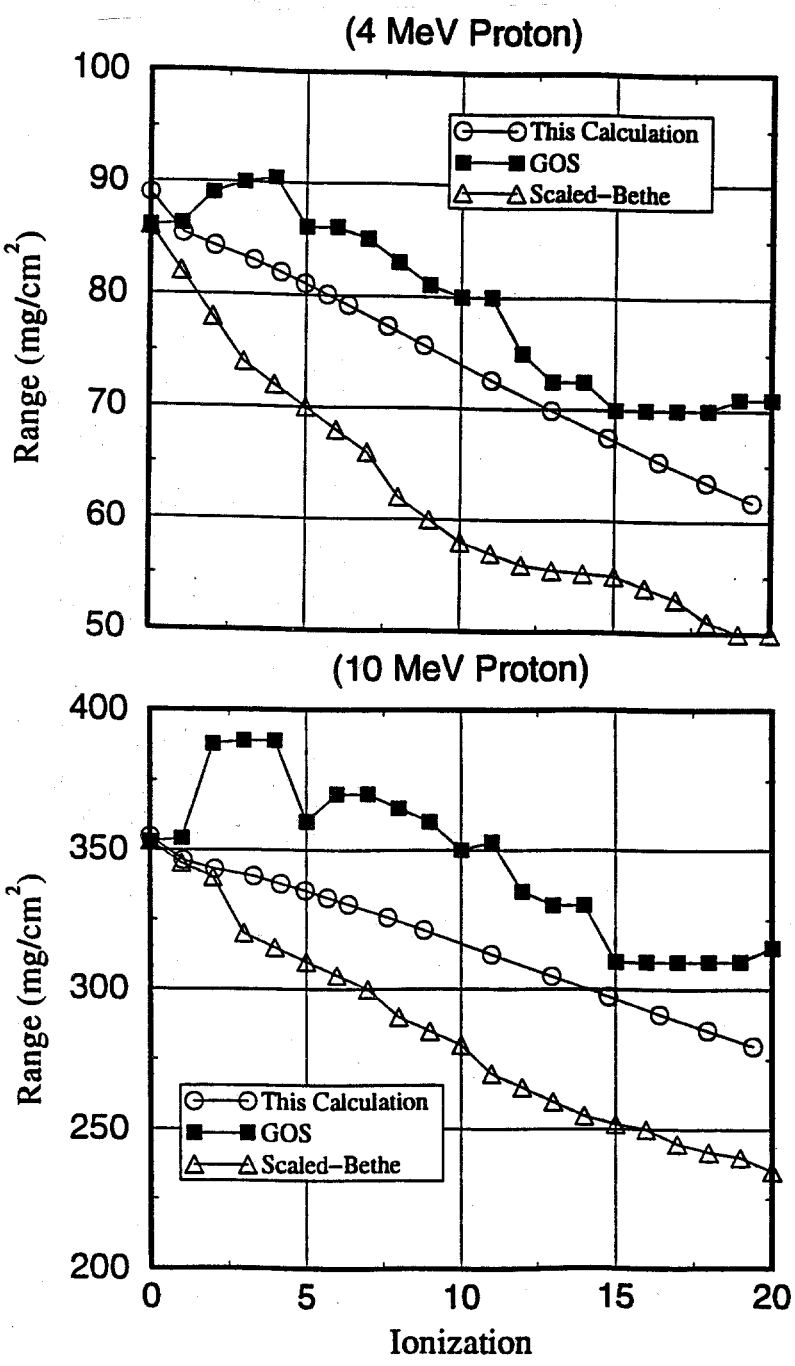

Figure 3.13. Stopping range of 4 MeV and 10 MeV protons in gold as a function of ionization state of the target. Results predicted by three different models are presented.

from electrons in excited states, which can be interpretated as 'quasi-bound' electrons in high density plasmas, is important in stopping power calculations and should be treated carefully.

3.6. Analytic Fits

In order to provide input data for hydrodynamic codes, the calculated stopping power data are fitted to simple analytic functions. The value of the total ion stopping power of a plasma target depends on the following parameters:

(1) charge of the projectile,
(2) energy (velocity) of the projectile,
(3) nuclear charge of the target,
(4) temperature of the target,
(5) particle density of the target.

Hence, an ideal data table for ion stopping powers would require 5 dimensions. In practice, a 5-dimensional table lookup is too complicated to implement. To reduce the complexity, the following points were considered:

A. A different data table is set up for each combination of projectile species and target plasma.
B. For given projectile and target conditions, the stopping-power is a very smooth function of projectile energy. A 10-parameter function is used for fitting the energy dependence.
C. Our calculations show that stopping-power and target charge state ($\bar{Z}$) is not in one-to-one correspondence. Hence, instead of using $\bar{Z}$, we do a curve fit for each (T, ρ) point.

At low energies, the electron stopping power is proportional to projectile velocity, while the high energy behavior of the stopping power is very well described by the Bethe formula [15]. Based on these asymptotic functional forms, we used the following functions to fit the energy dependence of stopping power, which is similar to that used by Ziegler, et al. [25]

$$\frac{dE}{dx} = A_1 \cdot E^{A_2} \qquad\qquad 0 < E \leq 0.1\, E_0$$

$$\left.\begin{aligned} &\frac{dE}{dx} = S_1 \cdot S_2/(S_1 + S_2) \\ &S_1 = A_3 \cdot E^{A_4} \\ &S_2 = (A_5/E) \cdot \ln\left(1 + A_6/E + A_7 E\right) \end{aligned}\right\} \quad 0.1\,E_0 < E \leq 10\,E_0$$

$$\frac{dE}{dx} = (A_8/E) \cdot \ln\left(1 + A_9/E + A_{10} E\right) \qquad E > 10\,E_0\,.$$

The fit is divided into three parts, one for the low energy regime ($E \leq 0.1\,E_0$), one for the high energy regime ($E > 10\,E_0$), and one for bridging the gap between low- and high-energy regimes. The energy E_0 corresponds to the maximum of the stopping power at each temperature and density point. It has been found that this fitting procedure works very well for all cases. Typical errors in the fit are only a few percent. Figure 3.14 shows a typical comparison of calculated data and its fitting curve. It can be seen that the fit well-represents the data over the entire energy range.

3.7. Summary

We have developed a model to study the energy deposition of an arbitrary ion in a material of arbitrary composition, density, and temperature. This model includes sophisticated treatments for electron density distribution of a atom in plasmas and a full Random Phase Approximation stopping number which extrapolates the zero temperature Lindhard stopping number to arbitrary temperatures. Therefore, it can accommodate a wide range of temperatures and densities relavant to ICF plasmas. We have shown that this model provides quite accurate ion stopping power in cold materials, including both low-Z and high-Z targets. For finite temperature plasmas, the model accounts for the stopping effects due to electrons in ground states, excited states and continuum states in a self-consistent manner. We have compared our calculated results of proton range in a gold plasma with those of the GOS model and scaled-Bethe model. Our results lie between the results of these two different models. No initial range lengthening feature is seen in our calculated results, which appears in GOS results. We concluded that this difference could be caused by the different treatments of less bounded electrons in excited states.

It is worthwhile pointing out that this model is in the framework of first-Born approximation for the projectile. For low energy heavy ions, the first-Born approximation is no longer appropriate and higher-order Born corrections should be included [20]. This can be done by directly including the Barkas term [28] and Bloch term [29] into our model. Further development of the model in this direction is currently under way.

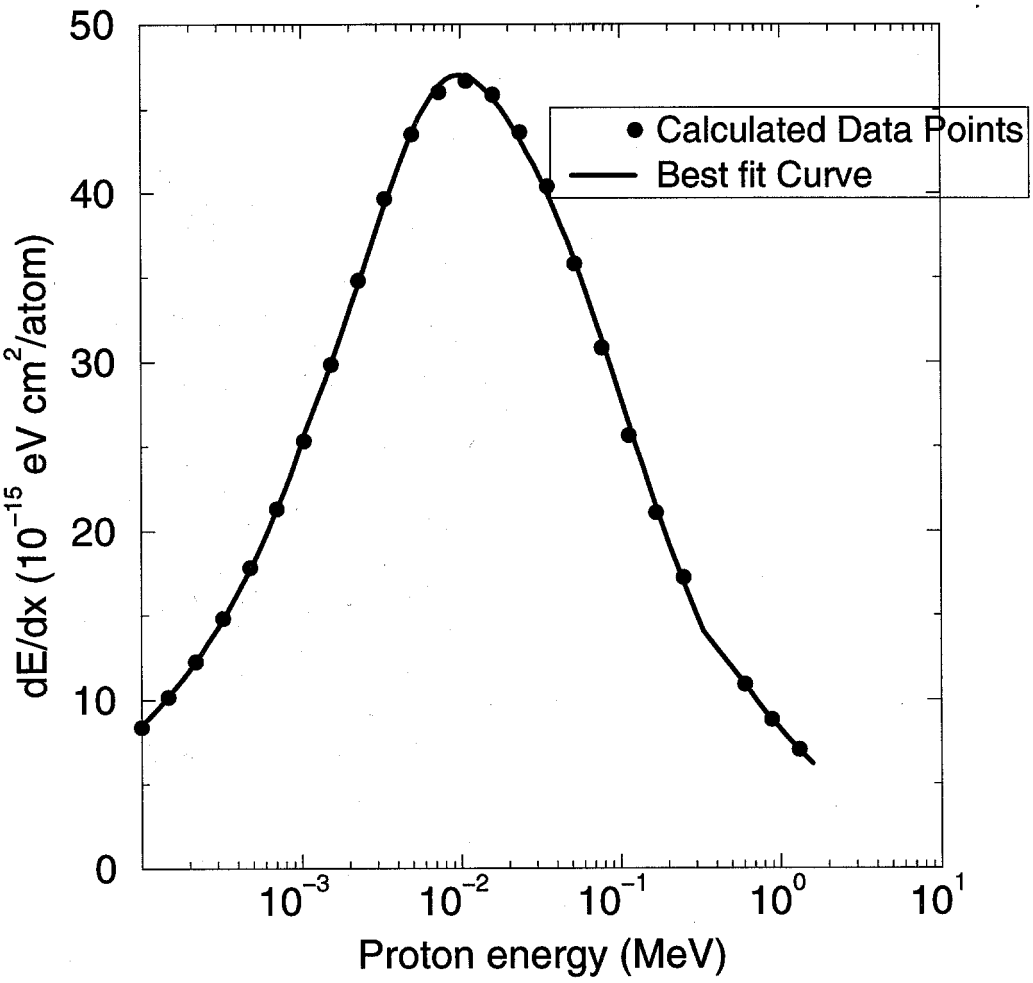

Figure 3.14. Stopping power for protons in an aluminum plasma having $T_e = 1$ eV, $\rho = 0.027$ g/cm^3. Both calculated data points and best fit curve are shown.

4. Equation of State (EOS) Tables for the KATACO Radiation-Hydrodynamics Code Based on Hybrid DCA/Muffin Tin Model

KALIF beam-target interaction experiments have been analyzed using KATACO, a radiation-hydrodynamics code, which calculates space- and time-dependent density-temperature profiles, $\rho(r,t)$ and $T(r,t)$. An essential input to KATACO is a knowledge of the material equation of state (EOS) which usually takes the form of pressure, p, and energy, E, as functions of ρ and T. The accurate simulation of experiments often requires high quality EOS data. For typical applications, one desires EOS data having an accuracy of $15\% - 20\%$ or better. Hydrodynamics codes can also encounter numerical difficulties (e.g., not conserving energy) if the EOS data is not thermodynamically consistent.

We have developed a hybrid model for calculating equation of state data for materials over a wide range of density and temperature conditions. In this hybrid EOS model, a detailed configuration accounting (DCA) approach is used for the low-density, high-temperature regime, while a "muffin-tin" model [19] is used for the high-density regime.

In the detailed configuration accounting approach, each isolated ion in the plasma is in equilibrium with free electrons. Plasma effects on each atomic system are considered as perturbations. Ionization distributions and level occupation numbers are obtained from detailed ionization balance calculations. The following contributions are included in the equations of state:

(1) the translational motions of ions and atoms,

(2) the effects of partially degenerate electrons,

(3) configuration effects from Coulomb interactions (Debye-Huckel corrections), and

(4) atomic internal contributions (excitations and ionizations).

The muffin-tin model is used to accurately compute the equation of state for high density plasmas. It is applicable to electrons on the zero-temperature isotherm as well as for any finite temperature. It has much of the simplicity of an isolated atom model but captures much of the physics of the band-structure model. In particular, it provides an accurate description of cohesion and the behavior of solids under compression. This model also describes an isolated atom or an ion in equilibrium with an electron gas in low density cases. Hence the muffin-tin model smoothly connects the high-density

electron degenerate regime and the low density plasma regime. This smooth connection provides thermodynamic consistency of calculated equations of state over a wide domain of temperatures and densities.

The hybrid model is designed to provide reliable equations of state over a wide range of plasma conditions. Figure 4.1 shows the results for energy and pressure isotherms for aluminum calculated using our hybrid model. In the low density regime, the nonlinear behavior due to atomic internal excitation/ionization is clearly seen. The cohesive, degenerate, and pressure ionization effects are observed for high density regime. Figure 4.2 shows a comparison of calculated shock Hugoniots with experimental data for Al and Au. It can be seen that the agreement is good.

The details of the physical basis for the equations used in the model have been presented elsewhere [2,19]. Here, we summarize the main features of the EOSOPA code, and the format of the EOS data tables.

EOSOPA is a program suite which consists of three computer codes:

(a) DCAOPA computes EOS data for low density plasmas using the DCA model;

(b) MFTEOS computes EOS data for intermediate- and high-density plasmas using the muffin-tin model; and

(c) JOINEOS connects the EOS data of DCAOPA and MFTEOS, checks the thermodynamic consistency of the EOS data, and generates the final EOS tables for radiation-hydrodynamics code.

The inputs are simply the material composition and basic atomic structure data (output from ATBASE). The outputs include pressure, energy, and their derivatives (e.g., $\frac{\partial p}{\partial \rho}$, $\frac{\partial p}{\partial T}$, $\frac{\partial E}{\partial T}$, etc.). Electron and ion pressures and energies are calculated separately. This is important for plasmas in which the two species have unequal temperatures. The calculated pressures and energies are smooth functions of ρ and T and satisfy the condition of thermodynamic consistency. A typical output file format is shown in Table 4.1.

Acknowledgement

Support for this work has been provided by the Forschungszentrum Karlsruhe, through Fusion Power Associates.

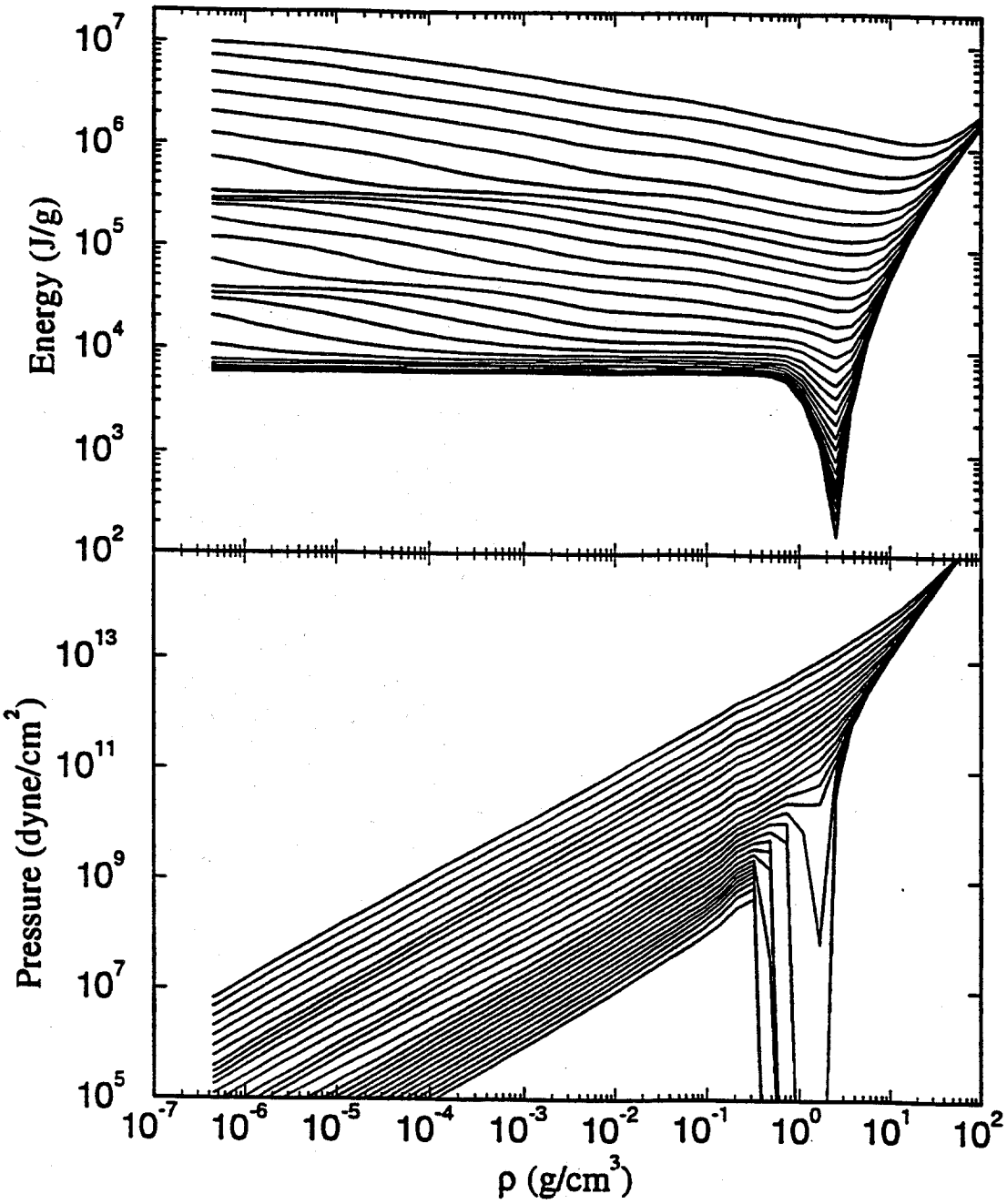

Figure 4.1. Energy and pressure isotherms calculated for aluminum using hybrid EOS model.

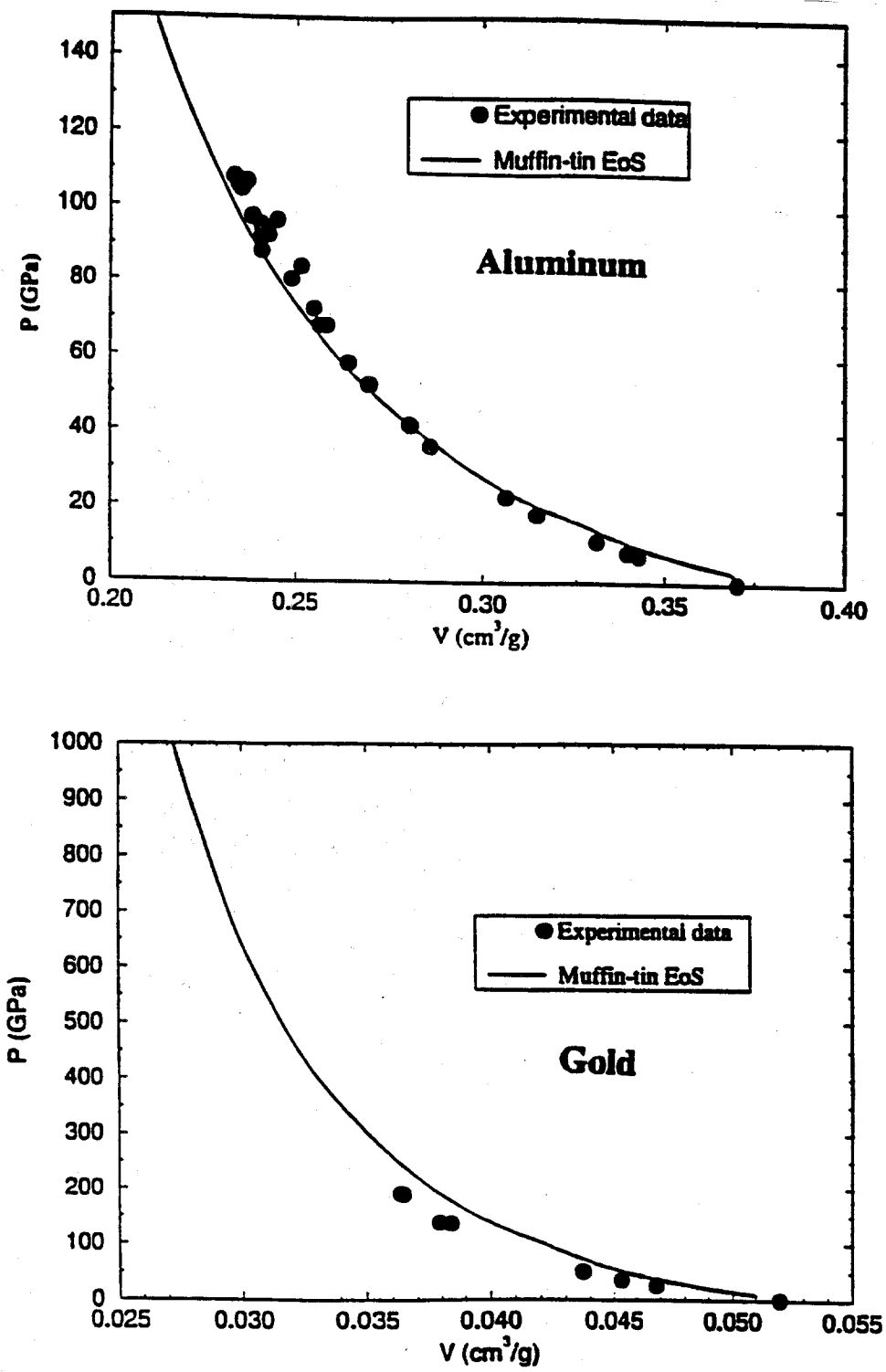

Figure 4.2. Comparison of calculated shock Hugoniots with experimental data for Al and Au.

Table 4.1. EOS And Opacity Data Table Format

Atomic number of species:	$A1, A2, ...$
Relative fraction:	$f1, f2, ...$
Number of temperature mesh points:	nT
Temperature mesh (eV):	$(T(i), i = 1, nT)$
Number of density mesh points:	nD
Density mesh (g/cm^3):	$(D(i),\ i = 1, nD)$
Solid density of the material (g/cm^3):	ρ_0
Number of photon energy groups:	nG
Group structure (eV):	$(Eg(i),\ i = 1, nG)$
Average charge state ($\bar{Z}$):	$((\bar{Z}(it, id), it = 1, nT), id = 1, nD)$
Total internal energy (J/g):	$((E_{\text{int}}(it, id), it = 1, nT), id = 1, nD)$
Heat capacity (J/g/eV):	$((dE_{\text{int}}/dT(it, id), it = 1, nT), id = 1, nD)$
$dE_{\text{int}}/d\rho$:	$((dE_{\text{int}}/d\rho(it, id), it = 1, nT), id = 1, nD)$
Ion energy:	$((E_{\text{ion}}(it, id), it = 1, nT), id = 1, nD)$
Electron energy:	$((E_{\text{ele}}(it, id), it = 1, nT), id = 1, nD)$
dE_{ion}/dT (J/g/eV):	$((dE_{\text{ion}}/dT(it, id), it = 1, nT), id = 1, nD)$
dE_{ele}/dT (J/g/eV):	$((dE_{\text{ele}}/dT(it, id), it = 1, nT), id = 1, nD)$
Ion pressure (J/cm^3):	$((P_{\text{ion}}(it, id), it = 1, nT), id = 1, nD)$
Electron pressure (J/cm^3):	$((P_{\text{ele}}(it, id), it = 1, nT), id = 1, nD)$
dP_{ion}/dT (J/cm^3/eV):	$((dP_{\text{ion}}/dT(it, id), it = 1, nT), id = 1, nD)$
dP_{ele}/dT (J/cm^3/eV):	$((dP_{\text{ele}}/dT(it, id), it = 1, nT), id = 1, nD)$
Rosseland mean opacity (cm^2/g):	$(((K_r(it, id, ig), it = 1, nT), id = 1, nD), ig = 1, nG)$
Planck emission mean opacity:	$(((K_e(it, id, ig), it = 1, nT), id = 1, nD), ig = 1, nG)$
Planck absorption mean opacity:	$(((K_a(it, id, ig), it = 1, nT), id = 1, nD), ig = 1, nG)$

References

1. MacFarlane, J.J., Moses, G.A., and Peterson, R.R., "BUCKY-1 – A 1-D Radiation-Hydrodynamics Code for Simulating Inertial Confinement Fusion High Energy Density Plasmas," University of Wisconsin Fusion Technology Institute Report UWFDM-984 (August 1995).

2. Wang, P., "EOSOPA – A Code for Computing the Equations of State and Opacities of High Temperature Plasmas with Detailed Atomic Models," University of Wisconsin Fusion Technology Institute Report UWFDM-933 (December 1993).

3. Boiko, V.A., Faenov, A. Ya, and Pikuz, S.A., *J. Quant. Spectrosc. Radiat. Transfer* **19**, 11 (1978).

4. Duston, D., and Davis, J., *Phys. Rev. A* **21**, 1664 (1980).

5. MacFarlane, J.J., "NLTERT – A Code for Computing the Radiative Properties of Non-LTE Plasma," Fusion Power Associates Report FPA-93-6 (December 1993).

6. Cowan, R.D., "The Theory of Atomic Structure and Spectra," University of California Press, Berkeley (1981).

7. Mehlhorn, T.A., *J. Appl. Phys.* **52**, 6522 (1981).

8. Wang, P., and Mehlhorn, T.A., "A Unified Self-Consistent Field Model for Ion Energy Deposition in Ion-Driven Inertial Confinement Fusion Targets," in preparation (1996).

9. MacFarlane, J.J., Wang, P., Bailey, J.E., Mehlhorn, T.A., Carlson, A., Johnson, D.J., and Haill, T., Presented at the Seventh International Workshop on Atomic Physics for Ion-Driven Fusion, Madrid, Spain (1995).

10. Wang, P., MacFarlane, J.J., and Moses, G.A., *Laser Part. Beams* **13**, 191 (1995).

11. MacFarlane, J.J., Wang, P., Bailey, J.E., Mehlhorn, T.A., and Dukart, R.J., *Laser Part. Beams* **13**, 231 (1995).

12. Deutsch, C., *Laser Part. Beams* **2**, 449 (1984).

13. Peter, T., and Meyer-Ter-Vehn, J., *Phys. Rev.* **A43**, 1998 (1990).

14. Nardi, E., Peleg, E., and Zinamon, Z., *Phys. Fluids* **21**, 574 (1978).

15. Bethe, H.A., Handbuch Der Physik, Edited by S. Flugge, Springer-Verlag, Berlin, Vol. 24, 273 (1933).

16. More, R.M., *Adv. Atomic Molec. Phys.* **21**, 305 (1985).

17. Linhard, J., Scharff, M., and Schiott, H.E., *Kgl. Danske Videnskab. Selskab. Mat. Fys. Medd.* **33**, 14 (1963).

18. Rousseau, C.C., Chu, W.K., and Powers, D., *Phys. Rev.* **A4**, 1066 (1970).

19. D.A. Liberman, *Phys. Rev.* **B20**, 4981 (1979).

20. Maynard, G., and Deutsch, C., *J. de Physique* **46**, 71 (1985).

21. Linhard, J., and Scharff, M., *Mat. Fys. Medd. Dan. Vid. Selsk.* **27**, 1 (1953).

22. Moruzzi, V.L., Janak, J.F., and Williams, A.R., Calculated Electronic Properties Of Metals, Pergamon Press, New York (1978).

23. Lafrate, G.J., Ziegler, J.F., and Nass, M.J., *J. Appl. Phys.* **51**, 984 (1980).

24. Mehlhorn, T.A., Peek, J.M., et al., J. de. Physique, Colloque C8, Supplement Au Noll **44**, 39 (1983).

25. Ziegler, J.F., Stopping Cross Sections For Energetic Ions In All Elements, Pergamon, New York, Vol. 5 (1980).

26. Northcliffe, L. and Schilling, R., *Nucl. Data Tables* **A7**, 233 (1970).

27. Mcguire, E.J., *Phys. Rev.* **A26**, 1871 (1982).

28. Barkas, W.H., Dyer, J.W., and Heckmann, H.H., *Phys. Rev. Lett.* **11**, 26 (1963).

29. Bloch, F., *Ann. Phys.* **16**, 285 (1933).